

Ares: A Mars model retrieval framework for ExoMars Trace Gas Orbiter NOMAD solar occultation measurements

George Cann^{a,b}, Ahmed Al-Refaie^b, Ingo Waldmann^b, Dave Walton^a, Jan-Peter Muller^a

^aImaging Group, Mullard Space Science Laboratory, Department of Space and Climate Physics, University College London, Holmbury St. Mary, Surrey, RH5 6NT, UK. Email: george.cann.15@ucl.ac.uk.

^bAstrophysics Group, Department of Physics and Astronomy, University College London, Gower Street, WC1E 6BT, UK.

Abstract

Ares is an extension of the TauREx 3 retrieval framework for the Martian atmosphere. Ares is a collection of new atmospheric parameters and forward models, designed for the European Space Agency's (ESA) Trace Gas Orbiter (TGO) Nadir and Occultation for Mars Discovery (NOMAD) instrument, Solar Occultation (SO) channel. Ares provides unique insights into the chemical composition of the Martian atmosphere by applying methods utilised in exoplanetary atmospheric retrievals, [Waldmann et al. \(2015\)](#), [Al-Refaie et al. \(2019\)](#). This insight may help unravel the true nature of CH₄ on Mars. The Ares model is here described. Subsequently, the components of Ares are defined, including; the NOMAD SO channel instrument function model, Martian atmospheric molecular absorption cross-sections, geometry models, and a NOMAD noise model. Ares atmospheric priors and forward models are presented, (i.e., simulated NOMAD observations), and are analysed, compared and validated against the Planetary Spectrum Generator, [Villanueva et al. \(2018\)](#).

Keywords:

Mars, CH₄, Ares, TauREx, NOMAD.

1. Introduction

In 2003, methane, CH₄, was tentatively detected in the Martian atmosphere, at 10 ppbv \pm 5, varying by up to 30 ppbv globally, [Formisano et al. \(2004\)](#), and 10 ppbv \pm 3 [Krasnopolsky et al. \(2004\)](#). CH₄ has, at most, a predicted photochemical lifetime of 300 years according to [Summers et al. \(2002\)](#). This implies that CH₄ in the Martian atmosphere should be uniformly distributed over Mars. However, non-uniform distributions of CH₄ have been observed, [Mumma et al. \(2009\)](#). This raises questions with regard to the source(s) and/or sink(s) of CH₄. Abiotic and biotic sources have been suggested to explain the detection, ranging from olivine serpentinization, [Morozova et al. \(2007\)](#), to methanogenesis by methanogenic archaea, [Allen et al. \(2006\)](#).

The Nadir and Occultation for Mars Discovery (NOMAD) instrument, [Vandaele et al. \(2015\)](#), [Robert et al. \(2016\)](#), onboard the European Space Agency's Exomars Trace Gas Orbiter (TGO) was designed to investigate the nature of methane, CH₄, on Mars, [Liuzzi et al. \(2019\)](#), [Mumma et al. \(2009\)](#). However, the arrival of TGO and subsequent science mission has detected no CH₄, with an upper limit of 0.05 ppbv, [Korablev et al. \(2019\)](#). In contrast, NASA's Curiosity Sample Analysis at Mars Tunable Laser Spectrometer instrument

(SAM-TLS), [Mahaffy et al. \(2012\)](#), has made multiple measurements of CH₄, including measuring an elevated CH₄ background of 7.2 ± 2.1 ppbv CH₄ over a 60-sol period in 2013, [Webster et al. \(2015\)](#). Subsequently, using SAM-TLS, [Webster et al. \(2018\)](#), determined a mean CH₄ abundance of 0.41 ± 0.16 ppbv, as well as a repeatable seasonal variation from 0.24 to 0.65 ppbv. Moreover, on 19th June 2019 it was reported that SAM-TLS measured a spike of 21 ppbv at Teal Ridge in Gale Crater, [NASA \(2019\)](#). Furthermore, the Planetary Fourier Spectrometer (PFS), [Formisano et al. \(1997\)](#), onboard Mars Express measured 15.5 ± 2.5 ppbv of CH₄, above Gale Crater on 16th June 2013, one day after SAM-TLS independently detected a CH₄ spike of 5.78 ± 2.27 ppbv, [Giuranna et al. \(2019\)](#). Since then PFS has detected no CH₄, [ESA \(2019\)](#). The discrepancy between surface measurements by SAM-TLS and orbital measurements from NOMAD and PFS, combined with the independent confirmation of detection of CH₄ by PFS, significantly constrains the mechanisms to corroborate the measurements.

Here we present a new retrieval scheme called Ares, an extension to the TauREx framework designed for TGO NOMAD Solar Occultation (SO) channel solar occultation measurements. Ares allows atmospheric sounding of the Martian atmosphere by applying methods developed originally for extracting tiny signals from noisy measurements of in exoplanetary atmospheric retrievals. This insight could help unravel the nature of CH₄ on Mars.

This paper is organized into distinct sections; firstly, the Ares model is described; subsequently, the components of Ares

Email addresses: george.cann.15@ucl.ac.uk (George Cann), ahmed.al-refaie.12@ucl.ac.uk (Ahmed Al-Refaie), ingo.waldmann@ucl.ac.uk (Ingo Waldmann), d.walton@ucl.ac.uk (Dave Walton), j.muller@ucl.ac.uk (Jan-Peter Muller)

and associated classes are defined, including; the NOMAD instrument function model, HITRAN 2016, [Gordon et al. \(2016\)](#), Martian absorption cross-sections, the geometry modules. Secondly, simulated NOMAD observations with Ares, are analysed, compared, and validated against the Planetary Spectrum Generator, [Villanueva et al. \(2018\)](#).

2. Ares outline

Ares is an extension of TauREx3, [Al-Refaie et al. \(2019\)](#), the 3rd generation of TauREx. TauREx, (Tau Retrieval for Exoplanets), [Waldmann et al. \(2015\)](#), is a fully Bayesian atmospheric retrieval framework that uses Nested Sampling, [Skilling et al. \(2006\)](#); [Feroz et al. \(2009\)](#), and Markov chain Monte Carlo (MCMC) methods to sample the full likelihood space of possible solutions. This allows TauREx to produce marginalised and conditional posterior distributions of forward model parameters, which can be used to map correlations between forward model parameters. This is advantageous over other planetary atmospheric retrieval frameworks that only find the *maximum a posteriori* (MAP) solution through Optimal Estimation, [Rodgers \(2000\)](#). The work presented here focuses on extending the TauREx3 radiative transfer forward models for Mars retrievals. We have named this TauREx 3 Mars extension module Ares.

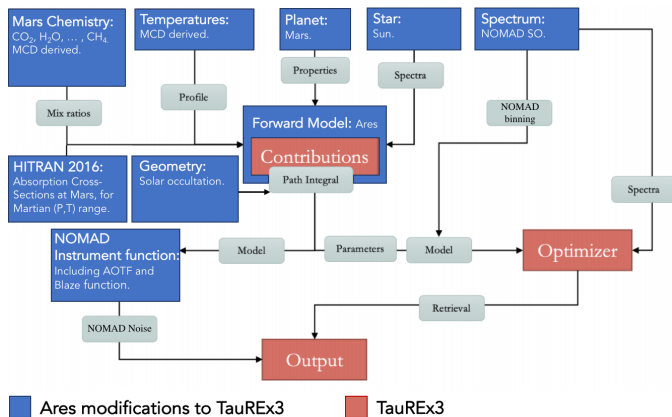


Figure 1: A flow diagram of Ares, modified from [Al-Refaie et al. \(2019\)](#). Red boxes represent TauREx3 modules. Blue boxes represent Ares modifications to TauREx3.

The NOMAD SO channel blaze function, acousto-optic tunable filter (AOTF) modules have been incorporated into the Ares forward model. Furthermore, Martian ellipsoidal and spherical geometry modules have been included in order to calculate the atmospheric layer line-of-sight (LOS) intersection points and corresponding path lengths, [Thomas et al. \(2018\)](#). A Mars Climate Database (MCD) Python library, pymcd, has been written and linked to the RTM, providing access to Martian vertical temperature, pressure and volume-mixing-ratio (VMR) profiles, [Forget et al. \(1999\)](#), [Millour et al. \(2018\)](#). Moreover, Martian absorption cross-sections have been generated using HITRAN 2016, [Gordon et al. \(2016\)](#), molecular line lists and ExoCross, [Yurchenko et al. \(2018\)](#), accounting for expected

Martian pressures, temperatures and CO₂ broadening, due to the CO₂-rich Martian atmosphere. Overall this enables Ares to produce simulated NOMAD SO channel transmission spectra.

2.1. NOMAD instrument

NOMAD is a high-resolution echelle grating spectrometer suite consisting of three channels; namely the Ultraviolet and Visible Spectrometer (UVIS), Solar Occultation (SO) and Limb, Nadir and Occultation (LNO), [Robert et al. \(2016\)](#). Each channel can operate in different geometry modes. UVIS functions in nadir and solar occultation mode geometries from 0.2-0.65 μm , SO functions in solar occultation geometry from 2.3-4.3 μm and LNO is dedicated to operating in limb and nadir geometries also from 2.3-4.3 μm . NOMAD is dedicated to investigate the composition of trace gas species in the Martian atmosphere, which can provide insights into present day geological and biological processes. NOMAD targets trace gas species including molecules such as, CO, HDO, C₂H₂, C₂H₄, H₂CO, H₂S, HCl, HCN, HO₂, NH₃, N₂O, NO₂, OCS and O₃. Additionally, NOMAD should be capable of determining the abundances of the isotopologues of the aforementioned species, that are of particular relevance to determining the biotic or abiotic nature of CH₄, [Vandaele et al. \(2015\)](#), [Robert et al. \(2016\)](#). These include the isotopologues of the Martian atmospheric carbon sources CO₂, CO, and CH₄, namely ¹³CO₂, ¹⁷OCO, ¹⁸OCO, ¹⁸CO₂, ¹³CO, ¹⁸CO, ¹²CH₄, ¹³CH₄ and CH₃D. Furthermore, NOMAD should be capable of determining the abundances of hydrocarbons such as C₂H₆ and sulfur sources, such as SO₂, [Yung et al. \(2018\)](#).

2.1.1. SO channel

This study will predominately focus on the NOMAD SO channel. NOMAD's SO channel covers 2.3-4.3 μm , for diffraction orders 96-225, with a resolving power of $\approx 20,000$ and a radio frequency input to the SO AOTF ranging between 12,300-31,100 kHz. For comparison, the LNO channel covers diffraction orders 108-220, with a resolving power of $\approx 10,000$ and a radio frequency input to the LNO AOTF ranging between 14,200-32,100 kHz. The NOMAD SO channel detector consists of a grid of 320 columns and 256 rows, along the spectral and spatial dimensions, respectively.

For NOMAD's SO channel, typically 24 rows of the detector range over an interval of approximately 7.5 km along the tangent height path, with a vertical sampling of 500 m, with the number of rows illuminated dependent on the Mars-Sun distance. Whilst extensive definitions of the instrument are given in [Neefs et al. \(2015\)](#), [Robert et al. \(2016\)](#) and [Liuzzi et al. \(2019\)](#), the temperature dependence of the AOTF and blaze functions are not reported. We obtained the requisite details on how to define the AOTF and blaze functions accounting for their temperature dependencies from the NOMAD Experiment to Archive Interface Document (EAICD), [Thomas et al. \(2018\)](#), and the NOMAD Datasets and Calibration Steps document, [Thomas et al. \(2019\)](#).

2.1.2. Calibration

NOMAD SO channel calibrations have been performed by, [Liuzzi et al. \(2019\)](#), [Thomas et al. \(2018\)](#), and include the conversion of detector pixel number and diffraction order to wavenumber, i.e. instrument spectral calibration, as well as instrument spectral resolution determination and thermal effects quantification. Moreover, measurements of the tuning relation have been performed to determine the relationship between the radio frequency applied to the SO channel AOTF and wavenumber at which the SO channel AOTF transfer function peaks.

The main product derived from the NOMAD instrument calibrations is an accurate model for NOMAD SO channel spectra. [Liuzzi et al. \(2019\)](#) and [Thomas et al. \(2018\)](#) note that different diffraction orders mix to produce the observed spectra, where between 15 - 50 % in a target order is contributed to by nearby orders, a property that increases with order number and AOTF frequency. [Liuzzi et al. \(2019\)](#) gives the functional relationship between pixel number p (from 0 to 319) wavenumber ν and order number m being modelled by a 2nd order polynomial. The retrieved coefficients for the aforementioned spectral calibration are given by,

$$\frac{\nu}{m} = F_0 + F_1 p + F_2 p^2. \quad (1)$$

Similarly the tuning relation is given by the following 2nd order polynomial,

$$\nu = G_0 + G_1 A + G_2 A^2, \quad (2)$$

where A is the AOTF frequency. The retrieved coefficients, G_0 , G_1 , G_2 , F_0 , F_1 and F_2 for the spectral calibration can be found in Table 1. and 2. of [Liuzzi et al. \(2019\)](#). Spectral calibration of NOMAD's SO channel is challenging due to the presence of a blaze function, an AOTF and the effects of temperature variation on these functions.

2.1.3. AOTF Transfer Function

NOMAD's SO channel AOTF is fundamentally a filter, as without it associating a particular absorption line to a particular wavelength would be challenging, as more than 100 diffraction orders would simultaneously fall on the detector, [Liuzzi et al. \(2019\)](#). The AOTF transfer function is given by the following equation.

$$TF(\nu, \nu_0, w, I_G, \rho_G, q, n) = F_{\text{sinc}} + F_{\text{gauss}} + F_{\text{cntmn}}, \quad (3)$$

where F_{sinc} , F_{gauss} and F_{cntmn} are given by,

$$F_{\text{sinc}}(\nu, \nu_0, I_0, w) = I_0 w^2 \frac{\left(\sin \frac{\pi(\nu - \nu_0)}{w}\right)^2}{\pi^2(\nu - \nu_0)^2} \quad (4)$$

$$F_{\text{gauss}}(\nu, \nu_0, I_G, \sigma_G) = I_G \exp\left(-\frac{(\nu - \nu_0)^2}{\sigma_G^2}\right) \quad (5)$$

$$F_{\text{cntmn}}(\nu, \nu_0, q, n) = q + n(\nu - \nu_0), \quad (6)$$

where ν_0 is the AOTF transfer function centre in cm^{-1} . I_0 is the sinc-squared function amplitude. Using prior coefficients

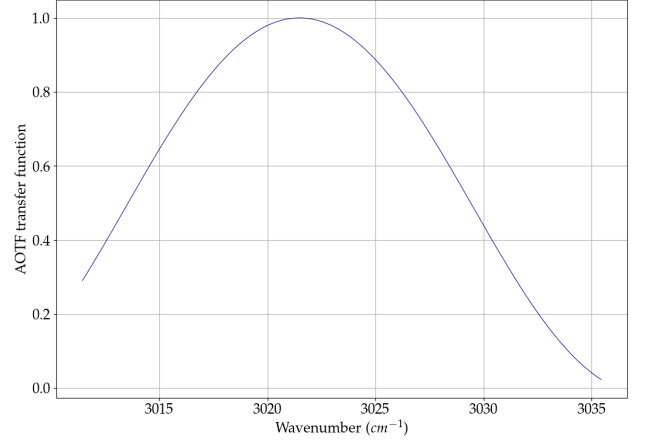


Figure 2: Ares derived plot of NOMAD SO channel AOTF transfer function intensity against wavenumber for diffraction order 134.

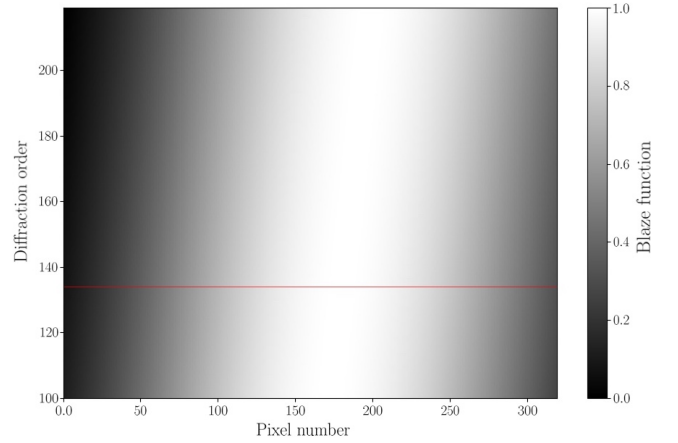


Figure 3: Ares derived map of NOMAD SO channel blaze function relative intensity against diffraction order and pixel number. For comparison see Figure 11. in [Liuzzi et al. \(2019\)](#). The red line corresponds to diffraction order 134.

and $\nu = G_0 + G_1 A + G_2 A^2$, ν_0 can be determined. w is the location of the first zero-crossing of the sinc-squared function. I_G is the Gaussian amplitude and σ_G the Gaussian standard deviation, q and n are the continuum offset parameters. Finally the relationship between w and the sinc-squared full-width half maximum (FWHM) is given by, $\text{FWHM} \approx 0.886w$. The set of coefficients G_0 , G_1 , and G_2 are the wavenumber-AOTF frequency calibration coefficients. These terms are included in the NOMAD EAICD with the same notation and can be found in Level 2 partially processed SO HDF5 files under `WnAOTF Coefficients`.

2.1.4. Blaze Function

A blaze function is included in Ares. [Liuzzi et al. \(2019\)](#) give the blaze function as,

$$F_{\text{blaze}}(p, p_0, w_p) = w_p^2 \frac{\left(\sin \frac{\pi(p - p_0)}{w_p}\right)^2}{\pi^2(p - p_0)^2} \quad (7)$$

where p is the pixel number (from 0 to 319), p_0 is the centre of the function in pixel units and w_p is the width of the blaze function. Note that in pixels w_p is equivalent to the free spectral range. This is defined by the properties of the grating and is equivalent to F_0 in equation 1. The blaze function p_0 is defined in the NOMAD EAICD by the following equation,

$$p_0(m) = I_0 + I_1 m, \quad (8)$$

where the coefficients I_0 and I_1 have been given as 150.80 and 0.22, respectively.

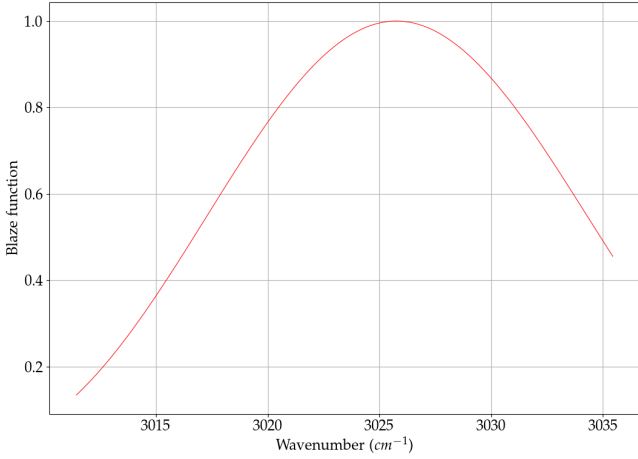


Figure 4: Ares derived plot of NOMAD SO channel blaze function intensity against wavenumber for diffraction order 134.

2.1.5. Spectral Continuum

The continuum in the NOMAD SO channel spectra is the result of the incoming continuum of the Sun, modified by the SO channel AOTF transfer function and the blaze function, Liuzzi et al. (2019). Subsequently, the intensity of each NOMAD SO channel pixel is modulated by the intensity of the SO channel AOTF transfer function and the blaze function. The continuum in NOMAD SO channel spectra, for a particular AOTF frequency, A , takes the form of the *Partial Elements Continuum*, $PEC(A)$, Liuzzi et al. (2019). Where $PEC(A)$, is given by,

$$PEC(A) = \sum_{j=m-\Delta m}^{m+\Delta m} PE(A, j). \quad (9)$$

$$PEC(A) = \sum_{j=m-\Delta m}^{m+\Delta m} AOTF(A, \nu_j) \cdot F_{\text{blaze}}(j, \nu_j) \cdot \text{gain}(j), \quad (10)$$

where $PE(A, j)$ represents a *Partial Element* of the $PEC(A)$. The *Partial Elements* for diffraction order 134 are shown in Figure 5 and Figure 6.

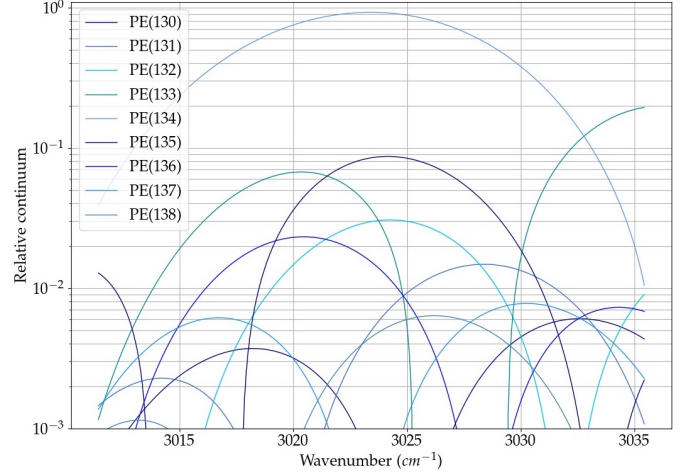


Figure 5: Ares derived relative flux contributions, *Partial Elements*, $PE(A, j)$ of the *Partial Elements Continuum*, $PEC(A)$, for $j \in [130, 138]$, for diffraction order 134, with Thomas et al. (2019) updated coefficients.

2.1.6. Observed Radiance

The radiance as observed by the NOMAD SO channel is given by Liuzzi et al. (2019) as,

$$R(A, \nu_m) = \sum_{j=m-\Delta m}^{m+\Delta m} AOTF(A, \nu_j) \cdot F_{\text{blaze}}(j, \nu_j) \cdot \text{gain}(j) \cdot R(j, \nu_j), \quad (11)$$

where $AOTF(A, \nu_j)$ is the AOTF transfer function at the AOTF frequency A , for spectral grid ν_j of diffraction order j . $F_{\text{blaze}}(j, \nu_j)$ is the blaze function of diffraction order j and the $\text{gain}(j)$ is the spectral average throughput in order j . NOMAD SO channel throughput has been characterised by NASA PSG team at NASA Goddard and is available on the PSG website. Liuzzi et al. (2019) states that by considering only orders close to the central order m , the $\text{gain}(j) \approx 1$ for all orders and therefore $R(A, \nu_m)$ can be rewritten as,

$$R(A, \nu_m) = \sum_{j=m-\Delta m}^{m+\Delta m} AOTF(A, \nu_j) \cdot F_{\text{blaze}}(j, \nu_j) \cdot R(j, \nu_j). \quad (12)$$

$R(j, \nu_j)$ encompasses all the *signal terms*, e.g. depending on observation type, planetary surface temperature, reflectance of the surface, aerosol extinction (in particular Martian dust and water ice) and scattering. With regard to CH_4 retrievals NOMAD SO channel diffraction order 134 is the order of most interest here, and so in this we are most interested in calculating $R(A, \nu_{134})$. As a side note, it is important to distinguish $R(j, \nu_j)$ from $R(A, \nu_m)$.

2.2. Geometry

In order to model NOMAD SO observations correctly, a module for computing a set of atmospheric-layer line of sight (LOS) intersection lengths is included in Ares. Thomas et al. (2016) use three types of Mars shape models to calculate the

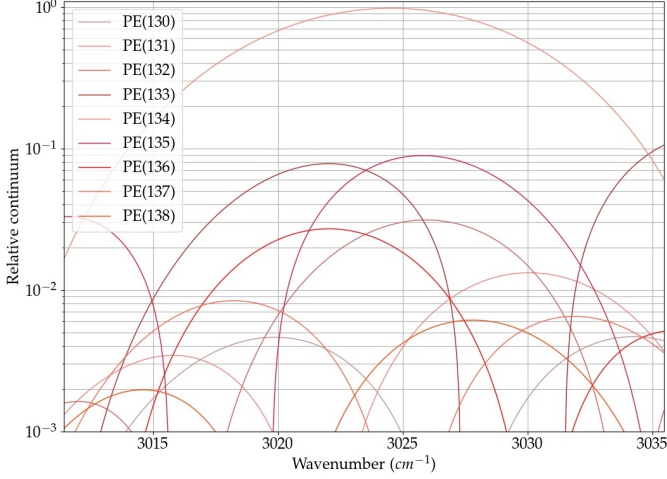


Figure 6: Ares derived relative flux contributions, *Partial Elements*, $PE(A, j)$ of the *Partial Elements Continuum*, $PEC(A)$, for $j \in [130, 138]$, for diffraction order 134, with Thomas et al. (2019) updated coefficients and AOTF transfer function temperature dependence.

aforementioned geometric parameters, these shape models include Ellipsoidal, Areoid and Surface. The ellipsoidal model is the most basic shape model used. Here, Mars is modelled as a tri-axial ellipsoid of radii: 3396.19 km \times 3396.19 km \times 3376.2 km. The areoidal model is not yet employed in Ares, due to the challenge of calculating the geodesic of the Areoid between (SubObsLat, SubObsLon) and (Point0, Point0).

For the areoid model, Mars is modelled to a *sea level*, where the gravitational and rotational potential is constant across the entire surface. This *zero level* is defined by MGS/MOLA (Mars Global Surveyor)/(Mars Orbiter Laser Altimeter) at a resolution of 4 pixels per degree (around 1.6 km). The surface model is the real surface elevation, calculated from a Digital Shape Kernel (DSK) by MGS/MOLA, again, at a resolution of 4 pixels per degree using Lemoine et al. (2001).

In solar occultation mode, the geometry is defined at the tangent point. The tangent point is the point on the Mars ellipsoid closest to the line of sight vector of each point. Each NOMAD shape model has a different tangent height variable, the following variables maintain NOMAD EAICD nomenclature, and are given by,

1. *TangentAlt*, is the height above the reference ellipsoid.
2. *TangentAltAreoid*, is the height above the areoid.
3. *TangentAltSurface*, is the height above the surface shape model.

Given the sublatitudes and sublongitudes of the TGO and tangent height, we are able to define an array of sublatitude and sublongitude points that define the path of solar irradiance to NOMAD. The shortest path on a spheroid, oblate spheroid, tri-axial ellipsoid and an areoidal surface will be different from one another. This said, we are not trying to find the shortest path on these surfaces, instead we are trying to find the intersection of the tangent point to spacecraft LOS with a set of spheroidal, oblate spheroidal, triaxial ellipsoidal and an areoidal surfaces.

In order to calculate the set of atmospheric-layer LOS intersection lengths, an altitude referencing system is employed. Again, maintaining EAICD nomenclature, the TGO altitude variables are given by,

1. *SurfaceRadius*, is the height of the surface model above the centre of Mars.
2. *SurfaceAltAreoid*, is the height of the surface above the reference areoid.
3. *ObsAlt*, is the range of the spacecraft from the centre of Mars.

The altitude of TGO above Mars' centre, is referenced in the NOMAD EAICD as *ObsAlt*, with the ellipsoidal, areoid and surface shape models sharing a common centre. For all geometry cases the following geometric attributes are set.

1. Assign the *Geometry* attribute for the TGO's observational altitude using *ObsAlt*.
2. Assign the *Point0* attribute for the tangent point altitude to the Martian surface using *TangentAltSurface*.
3. Assign the *Point0* attribute for the radius of the Martian surface relative to Mars' centre *SurfaceRadius*.
4. Assign the *Geometry* attribute for the TGO's sub-observation latitude point using *SubObsLat*.
5. Assign the *Geometry* attribute for the TGO's sub-observation longitude point using *SubObsLon*.
6. Assign the *Point0* attribute for the sub-latitude point for the tangent point, *Lat*.
7. Assign the *Point0* attribute for the sub-longitude point for the tangent point, *Lon*.

Point0 corresponds to the centre of the entire field of view of a NOMAD SO bin. A longitude and latitude grid of $n_{\text{lat-lon}}$ points is set; in this study $n_{\text{lat-lon}} = 10,000$. A fixed number of atmospheric layers, n_{layers} is also set such that $n_{\text{layers}} = 100$. Subsequently, the spacecraft's coordinates, relative to the centre of Mars, are calculated from,

$$x_s = r_s \cos(\varphi_s) \sin(\theta_s), \quad (13)$$

$$y_s = r_s \sin(\varphi_s) \sin(\theta_s), \quad (14)$$

$$z_s = r_s \cos(\varphi_s). \quad (15)$$

r_s is the TGO's observation altitude, *ObsAlt*, relative to Mars' centre, φ_s is the TGO's *SubObsLon* and θ_s is the TGO's *SubObsLat*. Similarly the tangent point coordinates, x_t , y_t and z_t , relative to Mars' centre, are calculated as, $x_t = r_t \cos(\varphi_t) \sin(\theta_t)$, $y_t = r_t \sin(\varphi_t) \sin(\theta_t)$, and $z_t = r_t \cos(\varphi_t)$. r_t is the tangent point's altitude, (*TangentAltSurface* + *SurfaceRadius*), relative to the centre of Mars, φ_t is the tangent point's sub-longitude, *Lon*, and θ_t is the tangent point's sub-latitude, *Lat*. Using Ares, a linear array of $n_{\text{lat-lon}}$ coordinates (x_i , y_i , z_i) are calculated using the tangent point and spacecraft coordinates (x_t , y_t , z_t) and (x_s , y_s , z_s). A linear array of distances from the centre of Mars are calculated $\forall i$ as,

$$r_i = \sqrt{x_i^2 + y_i^2 + z_i^2}. \quad (16)$$

The complexity of this challenge depends on the geometry assumed for the atmospheric layers. The following sections consider spherical, ellipsoidal and areoidal models.

2.2.1. Spherical

For the spherical case, the radius of Mars is set to $r_{\text{Mars}} = 3376.20$ km. Iterating over n_{layers} atmospheric layers, the goal becomes finding the points at which the LOS of NOMAD SO, defined by (x_t, y_t, z_t) and (x_s, y_s, z_s) intersects with the set of spherically defined atmospheric layers, (x_j, y_j, z_j) , and subsequently the distances between these points, dl_j . The path lengths, dl_j are then found by implementing an *intersection criteria*. These dl_j are subsequently passed to the Ares forward model to perform the radiative transfer integral.

2.2.2. Ellipsoidal

The ellipsoid, also called a tri-axial ellipsoid is a quadratic surface, which has a general equation given by,

$$\frac{x^2}{a^2} + \frac{y^2}{b^2} + \frac{z^2}{c^2} = 1. \quad (17)$$

where for NOMAD $a = 3396.19$ km, $b = 3396.19$ km and $c = 3376.20$ km. For the ellipsoidal case, the Mars' polar radius is set to $r_{\text{Mars,p}} = 3376.20$ km and its equatorial radius to $r_{\text{Mars,e}} = 3396.19$ km. Analytically, we can define a set of ellipsoidal atmospheric layers, however the flattening ratio of the ellipsoid, of which the ellipsoidal atmospheric layers are a subset, should be maintained. The flattening ratio of the ellipsoid is given by,

$$f = \frac{r_{\text{Mars,e}} - r_{\text{Mars,p}}}{r_{\text{Mars,e}}}. \quad (18)$$

Therefore the set of ellipsoids that define the ellipsoidal atmospheric layers are given by,

$$a_i = 3.39619 \times 10^6 + \Delta z_i, \quad (19)$$

$$b_i = 3.39619 \times 10^6 + \Delta z_i, \quad (20)$$

$$c_i = (3.39619 \times 10^6 + \Delta z_i)(1 - f). \quad (21)$$

Δz_i is derived from Ares `altitudeProfile` and represents the height of atmospheric layer i above the surface ellipsoid. Iterating over n_{layers} atmospheric layers, the goal becomes finding the points at which the LOS of NOMAD SO, defined by (x_t, y_t, z_t) and (x_s, y_s, z_s) intersects with the set of ellipsoidal defined atmospheric layers, (x_j, y_j, z_j) , and subsequently the distances between these points, dl_j . The dl_j are then found by implementing an *intersection criteria* and then passing this to the Ares forward model. Ares uses the `geographiclib` package (Karney, 2013) to calculate the ellipsoidal geodesic between (x_t, y_t, z_t) and (x_s, y_s, z_s) , utilising `Geodesic`, `InverseLine` and `Position`.

As stated previously, for the Areoid shape model, Mars can be modelled to a *sea level*, where the gravitational and rotational potential is constant across the entire surface. The areoidal model is not yet employed in Ares, due to the challenge of calculating the geodesic of the Areoid between (SubObsLat,

SubObsLon) and (Point0,Point0). This requires utilising `TangentAltAeroid`, `TangentAltAeroid`, `SurfaceRadius` and `SurfaceAltAeroid` attributes, with MGS/MOLA data. An approximation of the geodesic required could be achieved by calculating the geodesic, as is the case for Spherical or Ellipsoidal shape models and then mapping those latitude and longitude points to the Areoid.

2.3. Chemistry

2.3.1. Opacities

Ares utilises the spectroscopic line lists from the HITRAN 2016 (High Resolution Transmission) database (Gordon et al., 2016) to generate Martian absorption cross-sections. Through the Hitran Application Programming Interface (HAPI) (Kochanov, 2019), high resolution absorption cross-sections with `WavenumberStep = 0.001 cm-1`, have been generated for the Martian atmosphere for a range of NOMAD target species. Ares absorption cross-sections include, C_2H_4 , H_2CO , H_2S , HO_2 , NH_3 , NO_2 , OCS , O_3 , $^{12}\text{CH}_4$, $^{13}\text{CH}_4$, H_2O , $^{13}\text{CO}_2$ and $^{12}\text{CO}_2$. These absorption cross-sections account for expected Martian pressures, temperatures and CO_2 broadening, due to the CO_2 -rich Martian atmosphere. Using HAPI, we generate absorption cross-sections as a function for each molecule, isotopologue, pressures and temperatures for the required wavenumber range. Ares absorption cross-sections range in temperature and pressure from 100-300 K, increasing in increments of 10 K, and 0-600 Pa, increasing in increments of 10 Pa, respectively.

2.3.2. Mars Climate Database

The Mars Climate Database (MCD) is an output dataset derived from Global Climate Model (GCM) simulations of the Martian atmosphere using Mars orbiter data assimilation (Forget et al., 1999; Millour et al., 2018). In this study, the MCD, is used to provide atmospheric priors for use in Ares forward model simulations. In this study these atmospheric priors consist of constant vertical mixing ratio profiles for CO_2 , and H_2O . The MCD does not yet provide atmospheric data for CH_4 , and so the vertical mixing ratio profile for CH_4 is obtained for two cases provided by SAM-TLS. 7.2 ± 2.1 ppbv, from Webster et al. (2015), and has been adopted for the *high* methane concentration case and 0.41 ± 0.16 ppbv, from Webster et al. (2018), and for the *low* methane concentration case, representing the background concentration at Gale Crater.

3. Forward Modelling

In this section, we introduce the Ares transmission forward model, based on Waldmann et al. (2015) and the Tau model of Hollis et al. (2013). We link the Ares forward model to the aforementioned models; the NOMAD Instrument model, including *blaze* and *AOTF* functions, `NomadNoise`, `NOMAD Geometry` and the Mars Chemistry components, namely Martian absorption cross-sections and MCD atmospheric priors.

Forward modelling, is used with Inverse Modelling to obtain the best estimate of atmospheric properties. In the field

of atmospheric sciences, these best estimates are known as atmospheric retrievals. With regard to atmospheric retrievals, the forward model solves the Radiative Transfer Equation (RTE), Chandrasekar (1960), and defines the relationship between the so called state vector, \mathbf{x} , and measurement vector, \mathbf{y} , given by,

$$\mathbf{y} = \mathbf{F}(\mathbf{x}, \mathbf{b}) + \epsilon. \quad (22)$$

In the aforementioned equation \mathbf{b} is a parameter vector that includes all the forward model parameters that we do not seek to optimize. In the case of Ares, this could include Mars' surface emissivity, or H₂O and CO₂ ice cloud densities. ϵ is the forward model error and defines the error in a simulated measured signal due to the forward model, $\mathbf{F}(\mathbf{x}, \mathbf{b})$.

Inversion of $\mathbf{F}(\mathbf{x}, \mathbf{b})$, can then be used to obtain a statistical estimate of the state vector, \mathbf{x} , given measurement vector \mathbf{y} . Where \mathbf{x} represents the atmospheric priors and the measurement vector \mathbf{y} , represents a set of NOMAD SO channel transmission spectra.

If $\epsilon \neq \mathbf{0}$, then there exists an error in the Ares forward model, the model parameters or the observations. Under all realistic scenarios $\epsilon \neq \mathbf{0}$, and so the best estimate of the state vector that can be obtained, is a statistical estimate.

3.1. Beer-Bouguer-Lambert Law

The monochromatic intensity of radiation passing through a gas, $I_\lambda(z)$, is given by the *Beer-Bouguer-Lambert Law* as a function of atmospheric altitude z ,

$$I_\lambda(z) = I_\lambda(0)e^{-\tau_\lambda(z)}. \quad (23)$$

where λ is the wavelength of the radiation, $I_\lambda(0)$ the radiation intensity at the top of the atmosphere and $\tau_\lambda(z)$ the optical depth of the medium. For a given absorbing molecular species m we can define the optical depth to be the integral of the absorption cross-section $\zeta_m(\lambda)$, the column density $\chi_m(z)$, and $\rho_N(z)$ the number density, over the optical path length $l(z)$, given by,

$$\tau_{\lambda,m}(z) = 2 \int_0^{l(z)} \zeta_m(\lambda) \chi_m(z) \rho_N(z) dl. \quad (24)$$

The optical path length $l(z)$ is defined by the geometry of the transmission of radiation through the atmosphere. In the case of Mars $l(z)$ is provided by the Ares Geometry module. The total optical depth is given by the sum of the individual molecular species optical depths,

$$\tau_\lambda(z) = \sum_{m=1}^{N_m} \tau_{\lambda,m}(z), \quad (25)$$

N_m being the total number of absorbing molecular species. The monochromatic transmittance \mathcal{T}_λ is therefore given by,

$$\mathcal{T}_\lambda = e^{\tau_\lambda(z)}. \quad (26)$$

Therefore calculating \mathcal{T}_λ for all λ points in the spectral region of interest, e.g. the bandwidth of NOMAD SO channel diffraction order 134, with a *transmittance equivalent* of

$R(A, \nu_m)$ enables the simulation of NOMAD SO channel transmission spectra,

$$\mathcal{T}(A, \nu_m) = \frac{\sum_{j=m-\Delta m}^{m+\Delta m} AOTF(A, \nu_j) F_{\text{blaze}}(j, \nu_j) \text{gain}(j) \mathcal{T}(j, \nu_j)}{PEC(A)}. \quad (27)$$

For further details on forward modelling we refer the reader to Waldmann et al. (2015) and Hollis et al. (2013).

4. Analysis of simulated NOMAD observations with Ares

4.1. Bayesian analysis of planetary atmospheres

The Ares framework allows the user to select a range of optimisation routines to fit the atmospheric forward model to the data. In planetary science retrievals, the use of optimal estimation (Rodgers, 2000) is commonplace. Optimal Estimation (OE) calculates the maximum likelihood (ML) through a regularised matrix inversion of a Gaussian likelihood given prior constraints. OE methods yield excellent results in high signal-to-noise data regimes with good *a priori* knowledge of expected atmospheric forward-model parameters. However, in the case of low signal measurements and poorly constrained prior ranges, ML methods often insufficiently capture possible correlations in the likelihood surface for under-constrained retrievals. A typical example is atmospheric retrieval of extra-solar planet atmospheres where low-resolution data leads to significant correlations between measured trace-gas abundances. In these cases, it is necessary to solve for the full posterior probability distribution of the Bayesian argument.

Similarly, measuring trace-gas abundances at the detection limits of current instrumentation in the Martian atmosphere will require a complete understanding of possible correlations in the posterior distributions of the retrieval solution.

Following the definition of equation 22, we can state Bayes' Theorem as,

$$P(\mathbf{y}|\mathbf{x}, \mathcal{M}) = \frac{P(\mathbf{x}|\mathbf{y}, \mathcal{M})P(\mathbf{y}, \mathcal{M})}{P(\mathbf{x}, \mathcal{M})}. \quad (28)$$

\mathbf{x} is the observed spectrum (e.g. the NOMAD SO channel measurement), \mathbf{y} is the vector of atmospheric forward model parameters, and \mathcal{M} is the atmospheric forward model used. Hence, we want to compute the posterior distribution $P(\mathbf{y}|\mathbf{x}, \mathcal{M})$, describing the probability distribution of forward model parameters for a given spectrum and forward model. By default, we assume the likelihood, $P(\mathbf{x}|\mathbf{y}, \mathcal{M})$ to follow a Normal distribution,

$$P(\mathbf{x}|\mathbf{y}, \mathcal{M}) = \frac{1}{\epsilon \sqrt{2\pi}} \exp \left[-\frac{1}{2} \sum_{\nu} \left(\frac{x_\nu - \mathbf{F}_\lambda(\mathbf{y}, \mathbf{b})}{\epsilon_\nu} \right)^2 \right], \quad (29)$$

though other distributions can be specified in Ares. The prior distribution $P(\mathbf{y}, \mathcal{M})$ encapsulates the prior information for a given parameter and atmospheric model. In the case of Optimal Estimation, this prior must be Gaussian. In the Ares framework, the prior distribution can be any continuous probability

distribution, allowing for informative as well as uninformative priors (e.g. Jeffrey’s priors). By default, we utilise uninformative log-uniform prior distributions over retrieved trace-gas abundances to ensure a maximally data driven retrieval solution. Finally, we define the Bayesian Evidence as the integral of the likelihood and prior:

$$P(\mathbf{x}, \mathcal{M}) = \int P(\mathbf{y}, \mathcal{M})P(\mathbf{x}|\mathbf{y}, \mathcal{M})d\mathbf{y}. \quad (30)$$

The evidence allows for Bayesian model selection, i.e. the statistical comparison of the atmospheric with that of another. A commonly used scale for model significance is given by Kass and Raftery (1995).

4.2. Maximum a posteriori (MAP) Solution

The maximum a posteriori (MAP) solution is given by the maximum possible value of $P(\mathbf{y}|\mathbf{x}, \mathcal{M})$. The maximum of $P(\mathbf{y}|\mathbf{x}, \mathcal{M})$ is given by,

$$\nabla_{\mathbf{y}}P(\mathbf{y}|\mathbf{x}, \mathcal{M}) = \frac{\partial}{\partial \mathbf{y}}P(\mathbf{y}|\mathbf{x}, \mathcal{M}) = \mathbf{0}. \quad (31)$$

$\nabla_{\mathbf{y}} = \frac{\partial}{\partial \mathbf{y}}$ is the gradient operator in the state vector space and $\mathbf{0}$ is the zero vector in the state vector space. For uniform prior distributions, the MAP is equivalent to the maximum likelihood, and hence the result of Optimal Estimation. Whilst the MAP solution is informative, it does not reflect the full inter-parameter correlation possible in under constrained likelihoods. Similarly, by their definition, MAPs do not carry possibly diagnostic information on local maxima in the posterior distribution. By mapping the full posterior, we are able to derive a more robust understanding of the retrievability of trace gases at very low volume mixing ratios.

4.3. MCMC

Monte Carlo Markov Chain (MCMC) methods are often implemented in the field of exoplanetary science, whereby MCMC routines explore the likelihood space by means of a Markovian chain. TauREx3 provides an implementation of delayed rejection (DR) Adaptive MCMC (DRAM, Haario et al. (2006)). For further details we refer the reader to the literature; for brevity we provide a brief overview here. DRAM differs from the classical Metropolis-Hastings sampler Metropolis et al. (1953), Hastings (1970), Brooks et al. (2011), in that a DR algorithm is implemented and that an adaptive proposal distribution is calibrated using the co-variance of the sample path of the MCMC chain. MCMC does not typically sample the full likelihood volume and hence does not allow us to calculate the Bayesian evidence. Hence equation 28 is approximated as

$$P(\mathbf{y}|\mathbf{x}, \mathcal{M}) \propto P(\mathbf{x}|\mathbf{y}, \mathcal{M})P(\mathbf{y}, \mathcal{M}). \quad (32)$$

For implementation we refer the reader to Appendix A of Waldmann et al. 2015. TauREx3 runs several parallelised MCMC chains, in order to check convergence and increase the sampling of the likelihood space of possible solutions.

4.4. Nested Sampling

Nested Sampling (NS) algorithms Skilling et al. (2006) are frequently used in exoplanetary science for performing atmospheric retrievals and constitute the standard sampling method in Ares, Nestle, Barbary (2015) and MultiNest, Feroz et al. (2009). Whilst MCMC methods explore the entire likelihood space by means of a Markov chain, NS applies a general Monte Carlo analysis to periodically constrain ellipsoids that encompass spaces of highest likelihood. Through NS, the Bayesian partition function (i.e. the Bayesian evidence, E) can be calculated, allowing for exact model selection and a complete sampling of the likelihood. NS is the default sampler for the Ares framework.

5. Ares - Planetary Spectrum Generator Comparison

5.1. Validation

In order to validate Ares, the Ares forward model has been compared against NASA Goddard’s Planetary Spectrum Generator (PSG), Villanueva et al. (2018). The PSG is an extensive online radiative transfer suite that is capable of synthesising Martian NOMAD SO channel spectra. Like Ares, the PSG can utilise atmospheric priors from the MCD, Forget et al. (1999), Millour et al. (2018). Ares Martian transmittance and spectral radiance spectra, have been simulated using NOMAD observation metadata and compared against the PSG; running Ares and PSG forward models with mutual input variables.

This comparison is achieved through firstly populating PSG API *config* files with the same NOMAD observation metadata and priors, as is used for the Ares forward model simulations, such as tangent height, TGO observation altitude and atmospheric mixing ratio profiles. Following the population of the PSG configuration files a set of *curl* commands using the aforementioned *config* files are sent to the PSG API, for example:

```
curl -d type=rad -d whdr=n --data-urlencode
file@config.txt https://psg.gsfc.nasa.gov/api.php
-o config_output.txt
```

Setting *type=trn* in the *curl* command, with the radiation unit in the *config* file set to *rif*, returns the PSG transmittance simulation. Similarly, setting *type=rad* with the radiation unit in the *config* file set to *warm2cm* returns the PSG spectral radiance simulation. Ares, unlike the PSG, does not yet correct for Instrument Line Shape (ILS) ghosts, this is left to future work. The *config* files and *config-generator* associated with this comparison will be available in the Supplementary Material.

In all simulations, the vertical mixing ratio and temperature profiles are assumed to be constant and isothermal respectively. In Ares, the Sun is assumed to be a blackbody, with $T_{\odot} = 5778$ K. The wavenumber range of all simulations covers $\nu_{\min} = 2945$ cm^{-1} to $\nu_{\min} = 3130$ cm^{-1} , focusing on $\nu_{\min} = 3011$ cm^{-1} to $\nu_{\min} = 3035$ cm^{-1} , in order to cover NOMAD SO channel diffraction order 134, containing the CH_4 ν_3 band. The minimum and maximum atmospheric pressures are set to $p_{\min} = 1$ Pa and $p_{\max} = 600$ Pa respectively. In this initial comparison we do not include scattering or collision induced absorption.

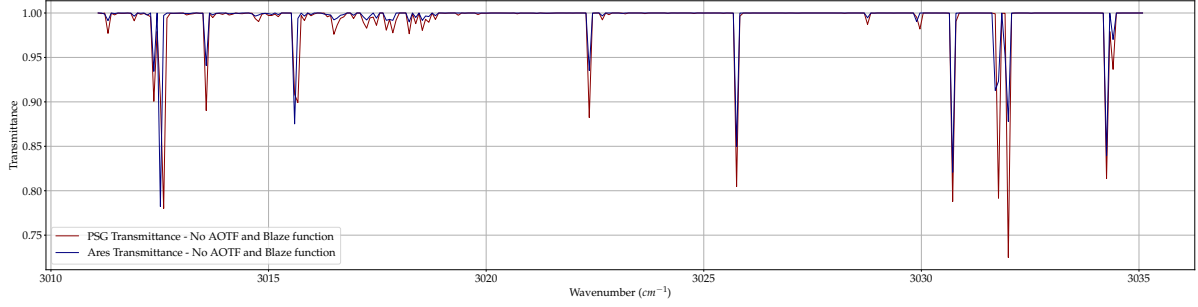


Figure 7: Ares PSG NOMAD SO channel solar occultation transmittance simulation comparison, covering the spectral range of diffraction order 134, 3011-3035 cm^{-1} , using mutual input variables, such as geometry and atmospheric priors. NOMAD AOTF and blaze function are not applied in this figure. Atmospheric priors and prior limits are provided in the top section of Table 1.

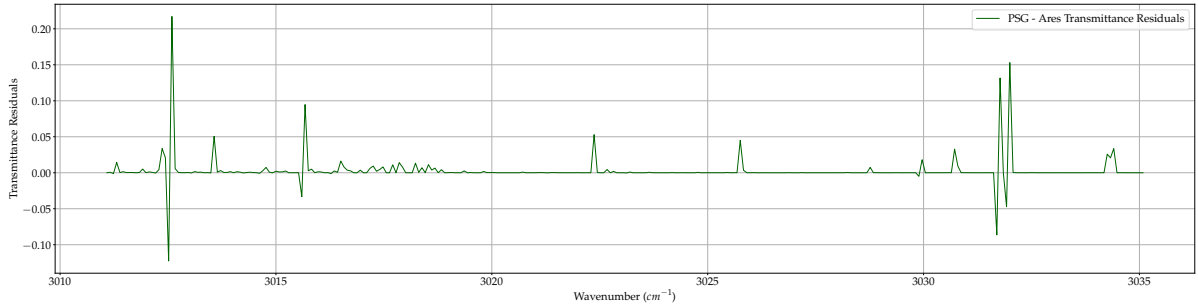


Figure 8: Ares PSG NOMAD SO channel solar occultation transmittance simulation residuals for Figure 7.

5.2. AOTF and Blaze function comparison

Whilst a transmittance simulation comparison between the PSG and Ares is possible, see Figure 7 and 8, a direct transmittance comparison with the NOMAD SO channel AOTF and blaze function applied is not. This is due to the PSG AOTF and blaze function transformations being inapplicable to transmittance simulations. Therefore, in order to correctly compare and validate Ares against the PSG, with and without the AOTF and blaze function applied, a conversion of Ares simulated transmittance to spectral radiance is required, or alternatively a conversion of the simulated PSG spectral radiance simulations, Figure 14, back to a transmittance simulation, Figure 11, after the PSG AOTF and blaze function transformations have been applied. In order to enable the AOTF and blaze function in the PSG, the generator telescope is set to AOTF. To disable the AOTF and blaze function the generator telescope is set to Single Dish, Villanueva et al. (2018).

5.3. Geometry comparison

For Ares, we observed that the simulated Ares transmittance spectra with the Ellipsoidal and Spherical geometry modules matches the PSG well with the same input variables. We observe, that the residuals between the Ellipsoidal and the PSG are smaller than when utilising the Spherical module. There are minor differences in the transmittance simulation absorption depths between, Ares and PSG, which could be due to using different absorption cross-sections or due to the differences in the Ares and PSG geometry module implementations.

Table 1: Ares - PSG forward model parameters and priors.

Parameter	Prior	Unit	Prior limits
H_2O	10^5	ppbv	$[1.0 \times 10^{-3}, 1.0 \times 10^7]$
CO_2	9.65×10^8	ppbv	$[9.0 \times 10^8, 9.8 \times 10^8]$
T	230	K	[130.0, 330.0]
$\text{CH}_{4,high}$	7.2	ppbv	$[1.0 \times 10^{-3}, 1.0 \times 10^2]$
$^{13}\text{CH}_4$	0.072	ppbv	$[1.0 \times 10^{-3}, 1.0 \times 10^7]$
OCS	1.0	ppbv	$[1.0 \times 10^{-3}, 1.0 \times 10^7]$
PH_3	1.0	ppbv	$[1.0 \times 10^{-3}, 1.0 \times 10^7]$
NH_3	1.0	ppbv	$[1.0 \times 10^{-3}, 1.0 \times 10^7]$

6. Results and Observations

Validating Ares through comparison to other established forward models is critical prior to progressing to perform Ares retrievals. The results of the Ares PSG forward model comparisons show that both models are generally in good agreement.

6.1. AOTF and Blaze function comparison

Figure 7, shows the Ares PSG NOMAD SO channel solar occultation transmittance simulation comparison, without applying AOTF and blaze function. We generally note minor differences in the absorption line depths. Figure 8, shows the transmittance residuals of Figure 7, with a maximum residual of 0.217 at 3012.59 cm^{-1} and a minimum residual of -0.123 at 3012.51 cm^{-1} . Whilst these residuals are significant, the

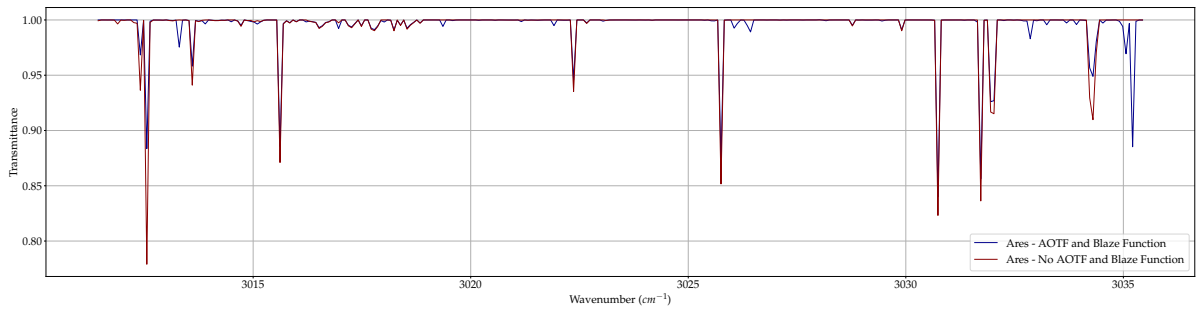


Figure 9: Ares NOMAD SO channel solar occultation transmittance simulation comparison, with and without AOTF and blaze function applied, covering the spectral range of diffraction order 134, 3011-3035 cm^{-1} .

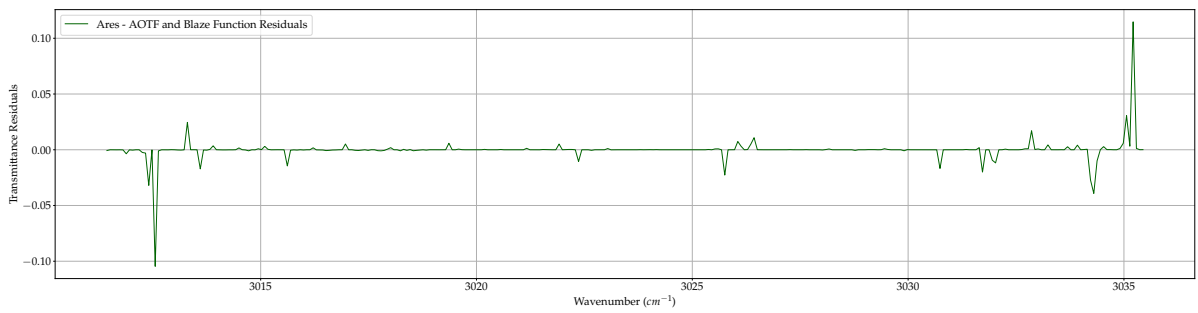


Figure 10: Ares NOMAD SO channel solar occultation transmittance simulation residuals for Figure 9.

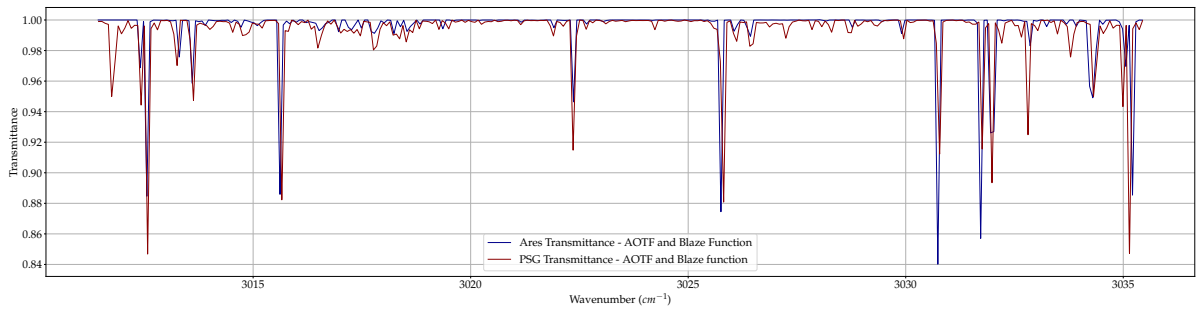


Figure 11: Ares PSG NOMAD SO channel solar occultation transmittance simulation comparison, with NOMAD SO channel AOTF and blaze function applied, covering the spectral range of diffraction order 134, 3011-3035 cm^{-1} .

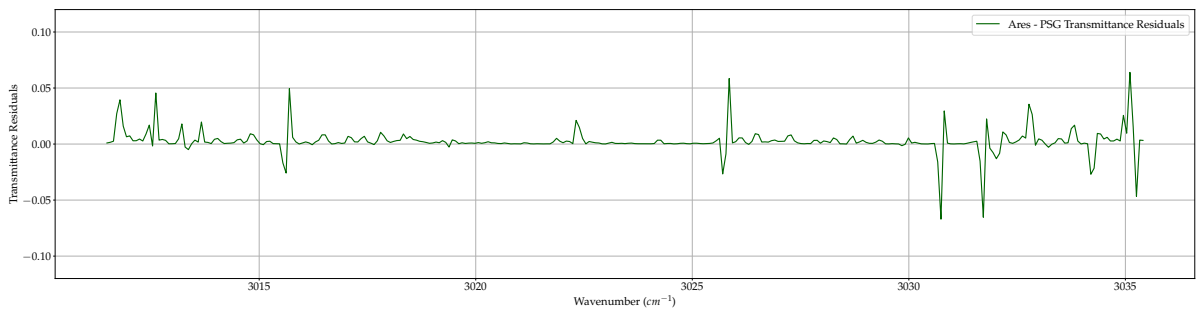


Figure 12: Ares PSG NOMAD SO channel solar occultation transmittance simulation residuals for Figure 11.

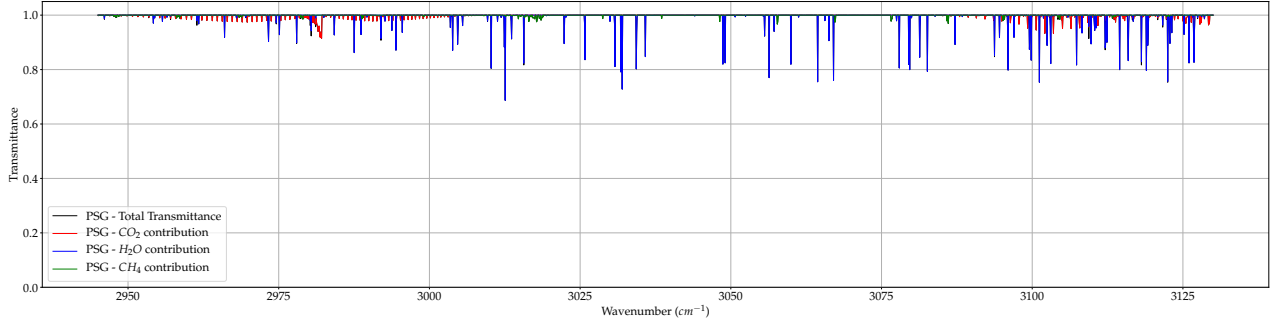


Figure 13: PSG NOMAD SO channel solar occultation simulated transmittance measurement for 2945-3130 cm^{-1} , showing molecular contributions of CO_2 , H_2O and CH_4 .

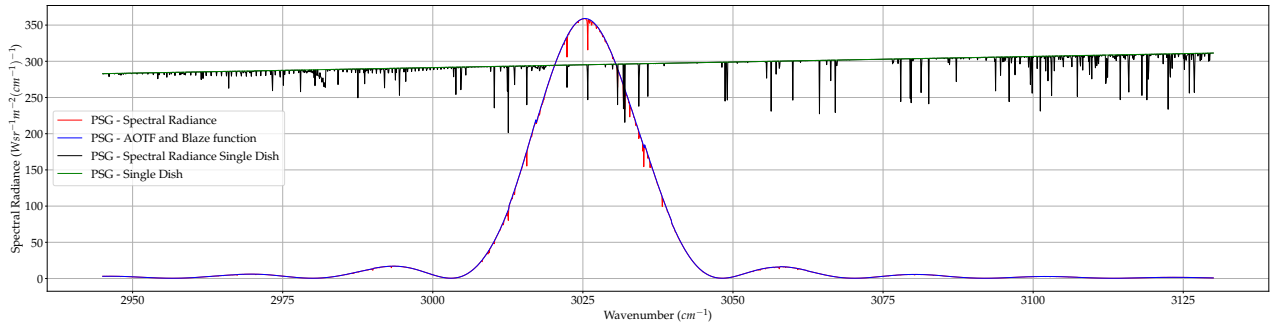


Figure 14: A graph of a PSG simulated spectral radiance measurement for NOMAD SO channel solar occultation for 2945 - 3130 cm^{-1} , with and without NOMAD SO channel AOTF and blaze function applied.

close proximity of the maximum and minimum residual, coupled with the similarity of absorption depths in Figure 7, suggests that these differences are due to minor discrepancies in the spectral line positions.

Figure 9, shows Ares NOMAD SO channel solar occultation simulated transmittance, with and without the AOTF and blaze function applied. Figure 10, shows the transmittance residuals of Figure 9, with a maximum residual of 0.115 at 3035.21 cm^{-1} and a minimum residual of -0.105 at 3012.56 cm^{-1} . Figure 11, shows the Ares PSG NOMAD SO channel solar occultation transmittance simulation comparison with the AOTF and blaze function applied. Figure 12, shows the transmittance residuals of Figure 11, with a maximum residual of 0.063 at 3035.11 cm^{-1} and a minimum residual of -0.067 at 3030.74 cm^{-1} . We observe that applying the AOTF and blaze function, the PSG and Ares, introduces absorption features, that are not present prior to AOTF and blaze function transformations. This exercise establishes that Ares and the PSG produce comparable results when the NOMAD SO channel AOTF and blaze function are applied.

6.2. Geometry comparison

We note a slight difference in absorption line depth between using Ares Spherical and Ellipsoidal geometry modules. However, this slight variation is dependent on the tangent height. The residuals between Ares geometry modules, across the simulated waveband, appears to decrease with increasing altitude.

This is to be expected, as the lower the altitude of the tangent point (or atmospheric LOS intersection point), the greater the difference between the calculated ellipsoidal and spherical path lengths. This difference, in turn is exacerbated by the increase in atmospheric density at lower altitudes. The residuals between Ares and PSG transmission spectra, across the simulated waveband, decrease with increasing altitude. This confirms the expectation, that the most challenging observations are those at lower altitudes Liuzzi et al. (2019).

6.3. Retrievals

Following the Ares PSG comparison, Ares marginalised and conditional posterior distributions have been generated for the aforementioned Ares simulated spectra Figure 11, shown in Figures 15 and 16. We have assigned uncertainties for each wavelength bin to give a signal-to-noise ratio of the maximum value expected by Liuzzi et al. (2019) of 1000 and utilised Nested Sampling, with Nestle set as the optimizer, with 200 live points.

Figure 15, shows an example of a set of Ares posterior distributions, retrieved using Ares, from a simulated NOMAD SO channel transmittance measurement. This retrieval covers diffraction order 134, using TGO observation 20180430-154925-1p0a-SO-A-I-134 metadata, with index (78,1), with tangent height 20.504 km. The jet colour scheme of the joint distributions is used to represent differences in probability density, whereby regions of high and low probability density are

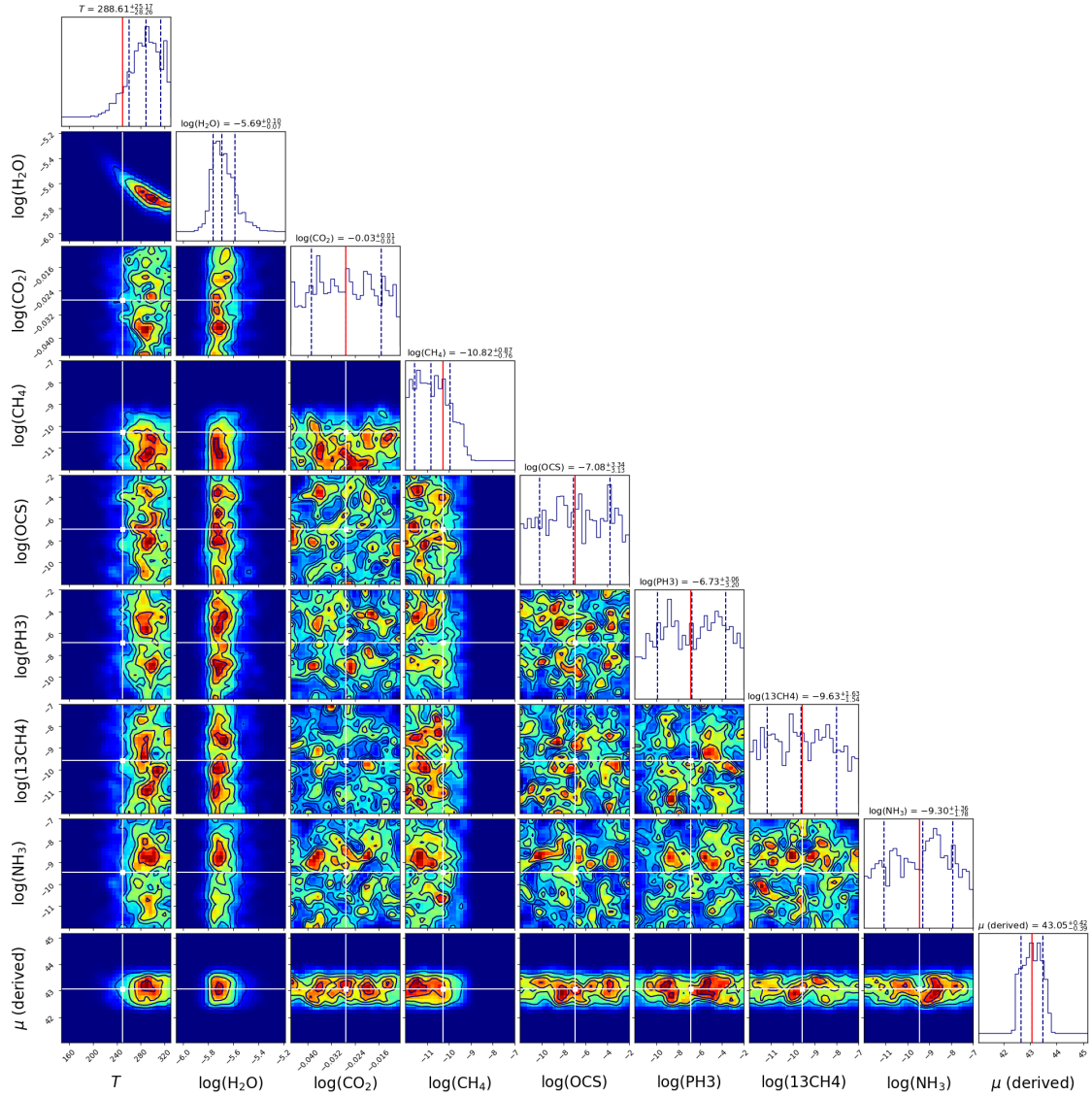


Figure 15: Posterior distributions of *simulated* NOMAD spectrum retrieved using Ares, for diffraction order 134, using observation: 20180430-154925-1p0a-SO-A-I-134 metadata, index (78,1), tangent height 20.504 km. Contours represent regions of high (red) and low (blue) probability density. Ares priors are represented by the red line in the marginalised distributions and as white cross hairs in the joint distributions. Dashed lines in the marginalised distributions represent are within σ_1 of the MAP estimate. We observe that the retrievals for OCS, PH₃ and ¹³CH₄ are poorly constrained. As expected, we note that retrievals of H₂O and temperature are correlated. Figure 15 was produced using the `corner.py` package, [Foreman-Mackey \(2016\)](#).

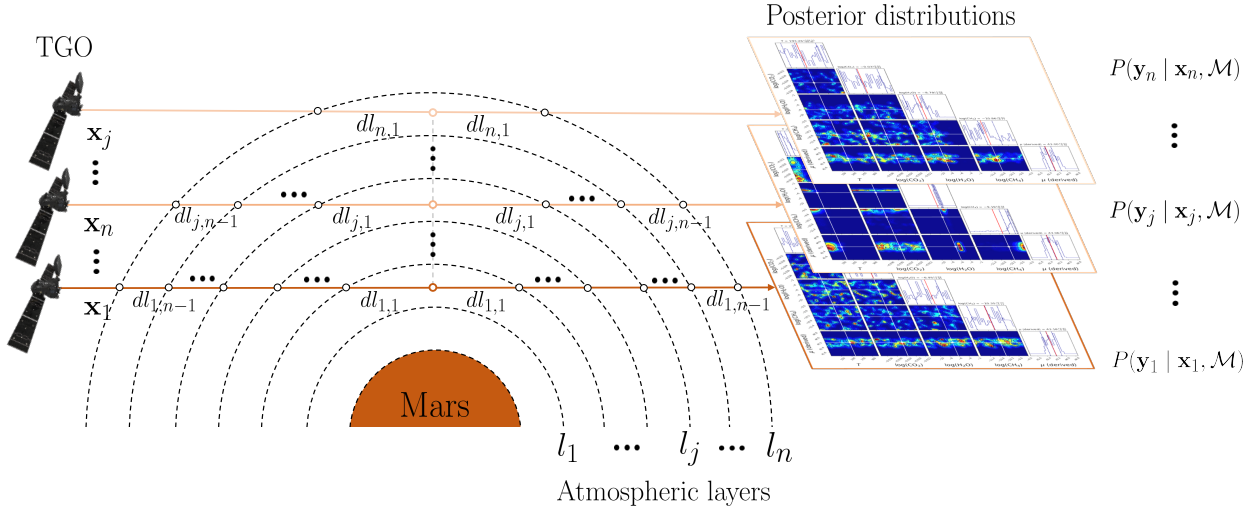


Figure 16: A schematic diagram of the TGO, Martian atmospheric layers and corresponding Ares a posterior distributions, mapping the exact statistical correlations between atmospheric parameters. Shown is a layer-by-layer retrieved atmosphere using simulated NOMAD spectra, for diffraction order 134, at three tangent heights, in the lower, middle and upper Martian atmosphere. We observe that the retrievals for lower tangent heights are strongly noise dominated while middle atmosphere retrievals produce tighter constraints.

represented within red and blue regions respectively. Ares priors are represented by the red line in the marginalised distributions and as white cross hairs in the joint distributions. As expected, we note that retrievals of H_2O and temperature are correlated. For this particular observation we find an upper limit of methane at $\log_{10}(\chi) = -10.82^{+0.87}_{-0.76}$ and no constraint of OCS, PH_3 , NH_3 and $^{13}\text{CH}_4$ beyond their prior bounds. We note that the tight prior bounds of CO_2 effectively constrain its abundance given the data and no further constraint within these priors is retrieved. The retrieved parameters are shown in Table 2.

Figure 16, visualises the advantages of utilising Ares to perform retrievals of forward model parameters, showing the TGO, Martian atmospheric layers and corresponding Ares a posterior distributions, for a set of NOMAD SO channel solar occultation measurements, \mathbf{x}_j . The set of probability density functions produced, $P(\mathbf{y}|\mathbf{x}, \mathcal{M})$, map the statistical correlations between atmospheric forward model parameters as function of altitude. Figure 16 shows a layer-by-layer retrieved atmosphere using simulated NOMAD spectra, for diffraction order 134, at three tangent heights, in the lower, middle and upper Martian atmosphere. We observe that retrievals for middle atmosphere tangent heights produce tighter constraints of probability density. This is expected as the optical depth is too high close to the surface and too low in the upper atmosphere. Whilst Ares is a simplified model of complex atmospheric phenomena, covering only a small subset of possible atmospheric conditions and TGO viewing geometries, it is nonetheless capable of gaining unique insight into the Martian atmosphere.

7. Conclusions

This research has described a novel retrieval framework, Ares, the Mars branch of TauREx 3 (Al-Refaie et al., 2019), designed for TGO NOMAD SO channel solar occultation measurements, the first in a series of papers. This research has characterised the instrument capabilities of the NOMAD instrument and the TauREx 3 based Ares model. In this research, Ares has been used to simulate transmittance and spectral radiance measurements and perform retrievals of typical Martian mixing ratio vertical profiles of CH_4 , H_2O , and CO_2 . The Ares forward model can simulate NOMAD spectra, including instrumental effects due to the blaze function, AOTF, as well as AOTF temperature dependence.

Ares and PSG simulated transmittance and spectral radiance measurements have been compared and are generally in good agreement, with marginalised and conditional posterior distributions of simulated and real data presented. We hope that Ares will help accelerate the use of advanced statistical sampling techniques, such as MCMC and Nested Sampling to fully explore the atmospheric forward model degeneracies encountered in low signal regimes where trace-gas abundances approach the instrument sensitivity floor. The work presented here will provide a new open-source tool to the planetary science community to study very faint spectral signatures in planetary atmospheres using a statistically robust framework.

Future forward model comparisons, made against the PSG, NEMESIS, Irwin et al. (2008), and ASIMUT-ALVL, Vandaele et al. (2006), will be used to further validate and refine Ares. Beyond Mars, Ares finds applications in the spectral analysis of Titan, Bellucci et al. (2009), the middle atmosphere of Venus,

Table 2: Ares forward model priors and retrieved parameters for Figure 16.

Parameter	Prior	Unit	Prior limits	Retrieved log(Parameters)
H ₂ O	10 ⁵	ppbv	[1.0 × 10 ⁻³ , 1.0 × 10 ⁷]	-5.69 ^{+0.07} _{-0.10}
CO ₂	9.65 × 10 ⁸	ppbv	[9.0 × 10 ⁸ , 9.8 × 10 ⁸]	-0.03 ^{+0.01} _{-0.01}
T	230	K	[130.0, 330.0]	288.61 ^{+28.26} _{-25.17}
CH _{4,high}	7.2	ppbv	[1.0 × 10 ⁻³ , 1.0 × 10 ²]	-10.82 ^{+0.87} _{-0.76}
¹³ CH ₄	0.072	ppbv	[1.0 × 10 ⁻³ , 1.0 × 10 ⁷]	-9.63 ^{+1.63} _{-1.54}
OCS	1.0	ppbv	[1.0 × 10 ⁻³ , 1.0 × 10 ⁷]	-7.08 ^{+3.34} _{-3.13}
NH ₃	1.0	ppbv	[1.0 × 10 ⁻³ , 1.0 × 10 ⁷]	-9.30 ^{+1.36} _{-1.78}
PH ₃	1.0	ppbv	[1.0 × 10 ⁻³ , 1.0 × 10 ⁷]	-6.73 ^{+3.06} _{-3.20}

Limaye et al. (2018), and the plumes of Enceladus, Waite et al. (2006).

8. Acknowledgements

We would like to thank the UK Space Agency for their support of this studentship through the Aurora Science Programme, STFC number 535385. We would like to thank The Royal Belgian Institute for Space Aeronomy (BIRA-IASB) for providing test NOMAD spectra, in particular Ian Thomas for help in understanding the intricacies of NOMAD. The NOMAD experiment is led by BIRA-IASB and assisted by Co-PI teams from Spain (IAA-CSIC), Italy (INAF-IAPS), and the United Kingdom (Open University). We would like to thank the LMD for providing the MCDv5.3 and Ehouarn Millour for installation help. This project has received funding from the European Research Council (ERC) under the European Union's Horizon 2020 Research and Innovation Programme (Grant agreement No. 758892, ExoAI). Furthermore, we acknowledge funding by the Science and Technology Funding Council (STFC) grants: ST/K502406/1, ST/P000282/1, ST/P002153/1 and ST/S002634/1.

9. Declaration of Interest Statement

The authors declare no competing financial interests.

10. Supplementary Material

Following publication of this work supplementary material associated with Ares and the Ares code will be provided open source, licensed under a BSD license, available at: <https://github.com/ucl-exoplanets/ares>.

References

- Allen, M., Sherwood Lollar, B., Runnegar, B., Oehler, D.Z., Lyons, J.R., Manning, C.E., Summers, M.E., 2006. Is Mars alive. *Eos. Trans. Am. Geophys. Union* 87, 433-439. <https://doi.org/10.1029/2006EO410001>.
- Al-Refaie, A.F., Changeat, Q., Waldmann, I.P., Tinetti, G., 2019. TauREx III: A fast, dynamic and extendable framework for retrievals. *Submitted to The Astrophysical Journal*. <https://arxiv.org/abs/1912.07759v1>.
- Barbary, K. 2015. Nestle, GitHub. <https://github.com/kbarbary/nestle>.
- Bellucci, A., Sicardy, B., Drossart, P., Rannou, P., Nicholson, P.D., Hedman, M., Baines, K.H., Burrati, B., 2009. Titan solar occultation observed by Cassini/VIMS: Gas absorption and constraints on aerosol composition, *Icarus*, Vol 201, Issue 1, 198-216. <https://doi.org/10.1016/j.icarus.2008.12.024>.
- Bohren, C. F., Huffman, D. R., 2007. Appendix A: Homogeneous Sphere (John Wiley and Sons), 477-482. <https://onlinelibrary.wiley.com/doi/pdf/10.1002/9783527618156.app2>.
- Brooks, S.P., Gelman, A., Jones, G.L., Meng, X.-L. eds, 2011. Handbook of Markov Chain Monte Carlo. Boca Raton, FL: Chapman and Hall/CRC Press.
- Chandrasekar, H. 1960. Radiative Transfer (New York: Dover Publications). <https://ui.adsabs.harvard.edu/abs/1960ratr.book...C/abstract>
- ESAs Mars orbiters did not see latest Curiosity methane burst, 2019. ESA. http://www.esa.int/Science_Exploration/.
- F. Feroz, M.P. Hobson, M. Bridges, 2009. MultiNest: an efficient and robust Bayesian inference tool for cosmology and particle physics, *Monthly Notices of the Royal Astronomical Society*, Vol 398, 1601-1614. <http://dx.doi.org/10.1111/j.1365-2966.2009.14548.x>.
- D. Foreman-Mackey, 2016. corner.py: Scatterplot matrices in Python, *Journal of Open Source Software*, 1(2), 24. <https://doi.org/10.21105/joss.00024>.
- Forget, F., Hourdin, F., Fournier, R., Hourdin, C., Talagrand, O., Collins, M., Lewis, S.R., Read, P.L., Huot, J-P., 1999. Improved general circulation models of the Martian atmosphere from the surface to above 80 km. *Journal of Geophysical Research*, Volume 104, Issue E10, 24155-24176. <https://doi.org/10.1029/1999JE001025>.
- Formisano, V., Moroz, V.I., Angrilli, F., Bianchini, G., Bussolletti, E., Cafaro, N., Capaccioni, F., Capria, M.T., Cerroni, P., Chionchio, G., Colangeli, L., Coradini, A., di Lellis, A., Fonti, S., Orfei, R., Palomba, E., Piccioni, G., Saggini, B., Ekonomov, A., Grigoriev, A., Gnedykh, V., Khatuntsev, I., Kiselev, A., Matsygorin, I., Moshkin, B., Nechaev, V., Nikolsky, Y., Patsaev, D., Russakov, A., Titov, D., Zasova, L., Blecka, M.I., Jurewicz, A., Michalska, M., Novosielski, W., Orleanski, P., Arnold, G., Hirsch, H., Driesher, H., Lopez-Moreno, J., Rodrigo, R., Rodriguez-Gomez, J., Michel, G., 1997. PFS: a fourier spectrometer for the study of martian atmosphere. *Adv. Space Res.* 19, 1277-1280. [https://doi.org/10.1016/S0273-1177\(97\)00282-2](https://doi.org/10.1016/S0273-1177(97)00282-2).
- Formisano, V., Atreya, S., Encrenaz, T., Ignatiev, N., Giuranna, M., 2004. Detection of methane in the atmosphere of Mars. *Science* 306, 1758-1761. <https://doi.org/10.1126/science.1101732>.
- Giuranna, M., Viscardi, S., Daerden, F., Neary, L., Etiope, G., Oehler, D., Formisano, V., Aronica, A., Wolkenberg, P., Aoki, S., Cardes-Ân-Moinelo, A., Mar-Ân-Yaseli de la Parra, J., Merritt, D., Amoroso, M., 2019. Independent confirmation of a methane spike on Mars and a source region east of Gale Crater. *Nature Geoscience*, 12, 326-332. <https://doi.org/10.1038/s41561-019-0331-9>.
- Gordon, I.E., Rothman, L.S., Hill, C., Kochanov, R.V., Tan, Y., Bernath, P.F., Birk, M., Boudon, V., Campargue, A., Chance, K., Drouin, B.J., Flaud, J.-M., Gamache, R.R., Hodges, J.T., Jacquemart, D., Perevalov, V.I., Perrin, A., Shine, K.P., Smith, M.A.H., Tennyson, J., Toon, G.C., Tran, H., Tyuterev, V.G., Barbe, A., Csaszar, A.G., Devi, V.M., Furtenbacher, T., Harrison, J.J., Hartmann, J.-M., Jolly, A., Johnson, T.J., Karman, T., Kleiner, I., Kyuberis, A.A., Loos, J., Lyulin, O.M., Massie, S.T., Mikhailenko, S.N., Moazzen-Ahmadi, N., Muller, H.S.P., Naumenko, O.V.,

- Nikitin, A.V., Polyansky, O.L., Rey, M., Rotger, M., Sharpe, S.W., Sung, K., Starikova, E., Tashkun, S.A., Vander Auwera, J., Wagner, G., Wilzewski, J., Wcislo, P., Yu, S., Zak, E.J., 2017. The HITRAN2016 molecular spectroscopic database. *J. Quant. Spectrosc. Radiat. Transf.* 203, 3-69. <https://doi.org/10.1016/j.jqsrt.2017.06.038>.
- Haario, H., Laine, M., Mira, A., Saksman, E. 2006. DRAM: Efficient adaptive MCMC, *Statistics and Computing*, 16, 339. <https://doi.org/10.1007/s11222-006-9438-0>.
- Hastings, W.K., 1970. Monte Carlo Sampling Methods Using Markov Chains and Their Applications, *Biometrika*, Vol. 57, No. 1, 97-109, 1970. <https://www.jstor.org/stable/2334940>.
- Hollis, M. D. J., Tessenyi, M., Tinetti, G., 2013. *Computer Physics Communications*, 184, 2351. <https://doi.org/10.1016/j.cpc.2013.05.011>.
- Irwin, P. G. J., Teanby, N. A., de Kok, R., Fletcher, L. N., Howett, C. J. A., Tsang, C. C. C., Wilson, C. F., Calcutt, S. B., Nixon, C. A., Parrish, P. D. (2008). The NEMESIS planetary atmosphere radiative transfer and retrieval tool. *JQSRT*, 109(6), 1136-1150. <https://doi.org/10.1016/j.jqsrt.2007.11.006>.
- Jacob, D.J., 2007. *Models of Atmospheric Transport and Chemistry, Lectures on Inverse Modeling*, Harvard, 1-24. http://acmg.seas.harvard.edu/education/jacob_lectures_inverse_modeling.pdf
- Karney, C.F.F. Algorithms for geodesics. *J Geod* 87, 43-55 (2013). <https://doi.org/10.1007/s00190-012-0578-z>.
- Kass, R.E. and Raftery, A.E., 1995. Bayes factors. *Journal of the American Statistical Association*, Vol 90, No. 430, 773-795, (1995). <http://www.jstor.org/stable/2291091>.
- Kochanov, R.V., 2019. HITRAN Application Programming Interface (HAPI), Harvard-Smithsonian Center for Astrophysics. https://hitran.org/static/hapi/hapi_manual.pdf
- Korablev, O., Vandaele, A.C., Montmessin, F., Fedorova, A.A., Trokhimovskiy, A., Forget, F., Lefèvre, F., Daerden, F., Thomas, I.R., Trompet, L., Erwin, J.T., Aoki, S., Robert, S., Neary, L., Viscardy, S., Grigoriev, A.V., Ignatiev, N.I., Shakun, A., Patrakee, A., Belyaev, D.A., Bertaux, Olsen, K.S., Baggio, L., Alday, J., Ivanov, Y.S., Ristic, B., Mason, J., Willame, Y., Depiesse, C., Hetey, L., Berkenbosch, S., Clairquin, R., Claudio, Q., Beeckman, B., Neefs, E., Patel, M.R., Bellucci, G., López-Moreno, J.-J., Wilson, C.F., Etiope, G., Zeleniy, L., Svedhem, H., Vago, J.L., The ACS and NOMAD Team, 2019. No detection of methane on Mars from early ExoMars Trace Gas Orbiter observations. *Nature*, 568, 517-520. <https://doi.org/10.1038/s41586-019-1096-4>.
- Krasnopolsky, V.A., Maillard, J.P., Owen, T.C., 2004. Detection of methane in the martian atmosphere: evidence for life. *Icarus* 172, 537-547. <https://doi.org/10.1016/j.icarus.2004.07.004>.
- Lee, J.-M., Heng, K., Irwin, P. G. J., 2007. Atmospheric retrieval analysis of the directly imaged exoplanet HR 8799b, *The Astrophysical Journal*, 778, 97. <https://doi.org/10.1088/0004-637x/778/2/97>.
- Lemoine, F., Smith, D., Rowlands, D., Zuber, M.T., Neumann, G.A., Chinn, D.S., Pavlis, D.E., 2001. An Improved Solution of the Gravity Field of Mars (GMM-2B) from Mars Global Surveyor. *Journal of Geophysical Research E: Planets*. 106. <https://doi.org/10.1029/2000JE001426>.
- Limaye, S.S., Mogul, R., Smith, D.J., Ansari, A.H., Slowik, G.P., Vaishampayan, P., 2018. Venus' Spectral Signatures and the Potential for Life in the Clouds, *Astrobiology*, Vol 18, Issue 9, 1181-1198. <https://doi.org/10.1089/ast.2017.1783>.
- Liuzzi, G., Villanueva, G.L., Mumma, M.J., Smith, M.D., Daerden, F., Ristic, B., Thomas, I., Vandaele, A.C., Patel, M.R., Lopez-Moreno, J.-J., the NOMAD team. Methane on Mars: New insights into the sensitivity of CH₄ with the NOMAD/ExoMars spectrometer through its first in-flight calibration. *Icarus* 321, 671-690. <https://doi.org/10.1016/j.icarus.2018.09.021>.
- Mahaffy, P.R., Webster, C.R., Cabane, M., Conrad, P.G., Coll, P., Atreya, S.K., Arvey, R., Barciniak, M., Benna, M., Bleacher, L., Brinckerhoff, W.B., Eigenbrode, J.L., Carignan, D., Cascia, M., Chalmers, R.A., Dworkin, J.P., Errigo, T., Everson, P., Franz, H., Farley, R., Feng, S., Frazier, G., Freissinet, C., Glavin, D.P., Harpold, D.N., Hawk, D., Holmes, V., Johnson, C.S., Jones, A., Jordan, P., Kellogg, J., Lewis, J., Lyness, E., Malespin, C.A., Martin, D.K., Maurer, J., McAdam, A.C., McLennan, D., Nolan, T.J., Noriega, M., Pavlov, A.A., Prats, B., Raaen, E., Sheinman, O., Sheppard, D., Smith, J., Stern, J.C., Tan, F., Trainer, M., Ming, D.W., Morris, R.V., Jones, J., Gundersen, A., Steele, A., Wray, J., Botta, O., Leshin, L.A., Owen, T., Battel, S., Jakosky, B.M., Manning, H., Squyres, S., Navarro-Gonzalez, R. McKay, C.P., Raulin, F., Sternberg, R., Buch, A., Sorensen, P., Kline-Schoder, R.,
- Coscia, D., Szopa, C., Teinturier, S., Baes, C., Feldman, J., Flesch, G., Forouhar, S., Garcia, R., Keymeulen, D., Woodward, S., Block, B.P., Arnett, K., Miller, R., Edmonson, C., Gorevan, S., Mumm, E., 2012. The Sample Analysis at Mars Investigation and Instrument Suite. *Space Sci. Rev.* 170, 401-478. <https://doi.org/10.1007/s11214-012-9879-z>.
- Metropolis, N., Rosenbluth, A.W., Rosenbluth, M.N., and Teller, A.H., 1953. Equation of State Calculations by Fast Computing Machines, *J. Chem. Phys.* 21, 1087, 1953. <https://doi.org/10.1063/1.1699114>.
- Millour, E., Forget, F., Spiga, A., Vals, M., Zakharov, V., Montabone, L., Lefèvre, F., F. Montmessin, Chaufray, J.-Y., López-Valverde, M.A., González-Galindo, F., Lewis, S.R., Read, P.L., Desjean, M.-C., Cipriani, F., the MCD development team, 2018. The Mars Climate Database (Version 5.3). Scientific Workshop: From Mars Express to ExoMars. https://www.cosmos.esa.int/documents/1499429/1583871/Millour_E.pdf.
- Morozova, D., Mohlmann, D., Wagner, D., 2007. Survival of Methanogenic Archaea from Siberian Permafrost under Simulated Martian Thermal Conditions. *Orig Life Evol Biosph* 37, 189-200, 2007. <https://doi.org/10.1007/s11084-006-9024-7>.
- Mumma, M.J., Villanueva, G.L., Novak, R.E., Hewagama, T., Bonev, B.P., DiSanti, M.A., Mandell, A.M., Smith, M.D., 2009. Strong release of Methane on Mars in northern summer 2003. *Science* 323, 1041-1045. <https://doi.org/10.1126/science.1165243>.
- Curiosity Detects Unusually High Methane Levels, 2019. NASA. <https://www.nasa.gov/feature/jpl/curiosity-detects-unusually-high-methane-levels>.
- Neefs, E., Vandaele, A.C., Drummond, R., Thomas, I.R., Berkenbosch, S., Clairquin, R., Delanoye, S., Ristic, B., Maes, J., Bonnewijn, S., Pieck, G., Equeter, E., Depiesse, C., Daerden, F., Ransbeeck, E.V., Nevejans, D., Rodriguez-Gomez, J., Lopez-Morez, J.-J., Sanz, R., Morales, R., Candini, G.P., Pastor-Morales, M.C., Aparicio del Moral, B., Jeronimo-Zafra, J.-M., Gomez-Lopez, J.M., Alonso-Rodrigo, G., Perez-Grande I., Cubas, J., Gomez-Sanjuan, A.M., Navarro-Medina, F., Thibert, T., Patel, M.R., Bellucci, G., De Vos, L., Lesschaeve, S., Vooren, N.V., Moelans, W., Aballea, L., Glorieux, S., Baeke, A., Kendall, D., De Neef, J., Soenen, A., Puech, P.-Y., Ward, J., Jamoye, J.-F., Diez, D., Vicario-Arroyo, A., Jankowski, M., 2015. NOMAD spectrometer on the ExoMars trace gas orbiter mission: part 1-design, manufacturing and testing of the infrared channels. *Appl. Opt.* 54, 8494. <https://doi.org/10.1364/AO.54.008494>.
- Robert, S., Vandaele, A.C., Thomas, I., Willame, Y., Daerden, F., Delanoye, S., Depiesse, C., Drummond, R., Neefs, E., Neary, L., Ristic, B., Mason, J., Lopez-Moreno, J.-J., Rodriguez-Gomez, J., Patel, M.R., Bellucci, G., 2016. Expected performances of the NOMAD/ExoMars instrument. *Planet. Space Sci.* 124, 94-104. <https://doi.org/10.1016/j.pss.2016.03.003>.
- Rodgers, C.D., 2000. *Inverse Methods for Atmospheric Sounding*, Vol. 2, World Scientific.
- Skilling, J., 2006. Nested sampling for general Bayesian computation. *Bayesian Anal.* 1, no. 4, 833-859. <https://projecteuclid.org/euclid.ba/1340370944>
- Summers, M.E., Lieb, B.J., Chapman, E., et al., 2002. Atmospheric biomarkers of subsurface life on Mars. *Geophys. Res. Lett.* 29, 2171. <https://doi.org/10.1029/2002GL015377>.
- Thomas, I.R., Vandaele, A.C., Robert, S., Neefs, E., Drummond, R., Daerden, F., Delanoye, S., Ristic, B., Berkenbosch, S., Clairquin, R., Maes, J., Bonnewijn, S., Depiesse, C., Mahieux, A., Trompet, L., Neary, L., Willame, Y., Wilquet, V., Nevejans, D., Aballea, L., Moelans, W., De Vos, L., Lesschaeve, S., Van Vooren, N., Lopez-Moreno, J.-J., Patel, M.R., Bellucci, G., the NOMAD Team, 2016. Optical and radiometric models of the NOMAD instrument part II: the infrared channels - SO and LNO. *Opt. Express* 24, 3790. <https://doi.org/10.1364/OE.24.003790>.
- Thomas, I., Vandaele, A.C., Neefs, E., 2018. NOMAD Experiment to Archive Interface Control Document, EXM-NO-ICD-AER-00001, Issue 1, Revision 11. BIRA-IASB. http://mars.aeronomie.be/en/exomars/observations/pages/EXM-NO-ICD-AER-00001-iss1rev11-EAICD_NOMAD_181026.pdf.
- Thomas, I., Vandaele, A.C., Neefs, E., 2019. HDF5 data pipeline, NOMAD Datasets and Calibration Steps. BIRA-IASB. https://nomad.aeronomie.be/ProjectDir/data/nomad_hdf5_datasets.pdf.
- Vandaele, A.C., Kruglanski, M., De Maziere, M., 2006. Modeling and retrieval of Atmospheric spectra using ASIMUT. European Space Agency, (Special Publication) ESA SP. <http://earth.esa.int/workshops/EPS-MetOp-RA0-2006proceedings/papers/p-vande.pdf>.

Vandaele, A.C., Neefs, E., Drummond, R., Thomas, I.R., Daerden, F., Lopez-Moreno, J.-J., Rodriguez, J., Patel, M.R., Bellucci, G., Allen, M., Altieri, F., Bolsee, D., Clancy, T., Delanoye, S., Depiesse, C., Cloutis, E., Fedorova, A., Formisano, V., Funke, B., Fussen, D., Geminale, A., Gerard, J.-C., Giuranna, M., Ignatiev, N., Kaminski, J., Karatekin, O., Lefevre, F., Lopez-Puertas, M., Lopez-Valverde, M., Mahieux, A., McConnell, J., Mumma, M., Neary, L., Renotte, E., Ristic, B., Robert, S., Smith, M., Trokhimovsky, S., Vander Auwera, J., Villanueva, G., Whiteway, J., Wilquet, V., Wolff, M., and The NOMAD Team, 2015. Science objectives and performances of NOMAD, a spectrometer suite for the ExoMars TGO mission. *Planet. Space Sci.* 119, 233-249. <https://doi.org/10.1016/j.pss.2015.10.003>

Villanueva, G.L., Smith, M.D., Protopapa, S., Faggi, S., Mandell, A.M., 2018. Planetary Spectrum Generator: An accurate online radiative transfer suite for atmospheres, comets, small bodies and exoplanets. *J. Quant. Spectrosc. Radiat. Transf.* 217, 86-104. <https://doi.org/10.1016/j.jqsrt.2018.05.023>.

Vispoel, B., Fissiaux, L., Lepère, M., 2019. CO₂-broadening coefficients in the ν₃ fundamental band of methane. *Journal of Molecular Spectroscopy*, Vol. 360, 1-6. <https://doi.org/10.1016/j.jms.2018.12.004>.

J. H. Waite Jr., Combi, M.R., Ip, W.H., Cravens, T.E., McNutt, R.L. Jr., Kasprzak, W., Yelle, R., Luhmann, J., Niemann, H., Gell, D., Magee, B., Fletcher, G., Lunine, J., Tseng, W.L., 2006. *Science* 311, 1419-1422. <https://doi.org/10.1126/science.1121290>.

Waldmann, I.P., Tinetti, G., Rocchetto, M., Barton, E.J., Yurchenko, S.N., Tennyson, J., 2015. Tau-REX I: A next generation retrieval code for exoplanetary atmospheres, *The Astrophysics Journal*, Volume 802, Number 2. <https://doi.org/10.1088/0004-637X/802/2/107>

Webster, C.R., Maha y, P.R., Atreya, S.K., Flesch, G.J., Mischna, M.A., Meslin, P.-Y., Farley, K.A., Conrad, P.G., Christensen, L.E., Pavlov, A.A., Martin-Torres, J., Zorzano, M.-P., McConnochie, T.H., Owen, T., Eigenbrode, J.L., Glavin, D.P., Steele, A., Malespin, C.A., Archer, P.D., Sutter, B., Coll, P., Freissinet, C., McKay, C.P., Moores, J.E., Schwenger, S.P., Bridges, J.C., Navarro-Gonzalez, R., Gellert, R., Lemmon, M.T., Team, theM.S., 2015. Mars methane detection and variability at Gale crater. *Science* 347, 415-417. <https://doi.org/10.1126/science.1261713>.

Webster, C.R., Maha y, P.R., Atreya, S.K., Moores, J.E., Flesch, G.J., Malespin, C., McKay, C.P., Martinez, G., Smith, C.L., Martin-Torres, J., Gomez-Elvira, J., Zorzano, M.-P., Wong, M.H., Trainer, M.G., Steele, A., Archer, D., Sutter, B., Coll, P.J., Freissinet, C., Meslin, P.-Y., Gough, R.V., House, C.H., Pavlov, A., Eigenbrode, J.L., Glavin, D.P., Pearson, J.C., Keymeulen, D., Christensen, L.E., Schwenger, S.P., Navarro-Gonzalez, R., Pla-Garcia J., Raffin, S.C.R., Vicente-Retortillo, A., Kahanpaa, H., Viudez-Moreiras, D., Smith, M.D., Harri, A.-M., Genzer, M., Hassler, D.M., Lemmon, M., Crisp, J., Sander, S.P., Zurek, R.W., Vasavada, A.R., 2018. Background levels of methane in Mars atmosphere show strong seasonal variations. *Science* 360, 1093-1096. <https://doi.org/10.1126/science.aag0131>.

Yung, Y.L., Chen, P., Neelson, K., Atreya, S., Beckett, P., Blank, J.G., Ehlmann, B., Eiler, J., Etiopie, G., Ferry, J.G., Forget, F., Gao, P., Hu, R., Kleinbohl, A., Klusman, R., Lefevre, F., Miller, C., Mischna, M., Mumma, M., Newman, S., Oehler, D., Okumura, M., Oremland, R., Orphan, V., Popa, R., Russell, M., Shen, L., Lollar, B.S., Staehle, R., Stamenkovic, V., Stolper, D., Templeton, A., Vandaele, A.C., Viscardy, S., Webster, C.R., Wennberg, P.O., Wong, M.L., Worden, J., 2018. Methane on Mars and Habitability: Challenges and Responses, *Astrobiology*, Vol 18, 1221-1242. <http://doi.org/10.1089/ast.2018.1917>.

Yurchenko, S.N., Al-Refaie, A.F., Tennyson, J., 2018. EXOCROSS: a general program for generating spectra from molecular line lists. *Astronomy and Astrophysics*, Vol. 614, A131. <https://doi.org/10.1051/0004-6361/201732531>.

et al. (2015), the noise of the channels is the sum of the different noise contributions, given by the following,

$$N = N_{\text{dark}} + N_{\text{ro}} + N_{\text{quant}} + N_{\text{shot}} + N_{\text{tb}}. \quad (\text{A.1})$$

The following list explains in detail the aforementioned sources of noise:

1. The *dark current noise*, N_{dark} , is a fixed source of noise, measured in electrons per pixel per second. The assumed value of the dark current for NOMAD IR channels is 6000 e⁻pixels⁻¹s⁻¹. N_{dark} is given by,

$$N_{\text{dark}} = \sqrt{6000\Delta t}. \quad (\text{A.2})$$

where Δt is the integration time. Integration time meta-data is given with NOMAD observations.

2. The *readout noise*, N_{ro} , is a fixed source of noise due to the detector readout, measured in pixels per second per observation. For the MARS-MW detector, in SO and LNO channels, N_{ro} is given by,

$$N_{\text{ro}} \approx 1000 \text{ e}^- \text{pixel}^{-1}. \quad (\text{A.3})$$

3. The *thermal background noise*, N_{tb} , is the noise in the detector produced by the thermal background. N_{tb} is given by,

$$N_{\text{tb}}(i) = \sqrt{S_{\text{tb}}(i)}. \quad (\text{A.4})$$

where $S_{\text{tb}}(i)$ represents the electrons generated in detector pixel i due to thermal emission coming from the instrument. Whilst N_{tb} is challenging to simulate, Liuzzi et al. (2019), provides a set of expected thermal background noise values given a set of NOMAD instrument temperatures. At 263K $N_{\text{tb}} = 1.5 \times 10^7 \text{ e}^- \text{s}^{-1}$, at 273K $N_{\text{tb}} = 3.0 \times 10^7 \text{ e}^- \text{s}^{-1}$ and at 283K $N_{\text{tb}} = 4.0 \times 10^7 \text{ e}^- \text{s}^{-1}$.

4. The *quantization noise*, N_{quant} , is due to the finite number of bits used for analogue-to-digital encoding of the signal detected by the detector chip. N_{quant} is calculated as,

$$N_{\text{quant}} = \frac{S_{\text{FWC}}(i)}{\sqrt{12} \cdot 2^{\text{nbits}} \left(\frac{\Delta V_{\text{ADC,usable}}}{\Delta V_{\text{ADC,max}}} \right)}. \quad (\text{A.5})$$

$S_{\text{FWC}}(i)$ is the full well capacity of the detector pixel i . $\Delta V_{\text{ADC,usable}}$ corresponds to the usable voltage range of the analogue-to-digital converter and $\Delta V_{\text{ADC,max}}$ is the converters maximum voltage range. For NOMAD $S_{\text{FWC}}(i) = 3.7 \times 10^7$, $\Delta V_{\text{ADC,max}} = 5 \text{ V}$, $\Delta V_{\text{ADC,usable}} = 3.78 \text{ V}$ and $\text{nbits} = 14$. As all terms are defined, N_{quant} can be calculated as,

$$N_{\text{quant}} = \frac{3.7 \times 10^7}{\sqrt{12} \cdot 2^{14} \left(\frac{3.78}{5.0} \right)} = 862.3 \text{ e}^- \text{pixel}^{-1} \text{ (1d.p.)}. \quad (\text{A.6})$$

5. The *shot noise*, N_{shot} , is the noise resulting from the signal photons impacting the detector. N_{shot} is given by,

$$N_{\text{shot}} = \sqrt{S_{\text{electrons}}(i)}. \quad (\text{A.7})$$

Appendix A. NOMAD Noise Model

Real NOMAD SO channel data will include noise, therefore in order to test the ability of Ares to perform retrievals on simulated NOMAD SO observations, a module for computing the expected noise is included. A fundamental component of Ares is the `NomadNoise` class. This class considers all the sources of noise present within NOMAD observations. As stated in Neefs

In the model applied, [Thomas et al. \(2016\)](#), flux is calculated one diffraction order at a time. Flux outside the gratings full spectral range are ignored as they are accounted for by the adjacent orders. The number of electrons $S(i)$ generated in a detector pixel during integration time Δt is given by,

$$S_{\text{electrons}}(i) = \frac{\lambda_i}{hc} \tau_{\text{det}}(\lambda_i) E_Q(\lambda_i) S(\lambda_i) \Delta t \quad (\text{A.8})$$

λ_i is the wavelength corresponding to pixel i , $E_Q(\lambda_i)$ is the quantum efficiency of the detector and τ_{det} is the sensitivity of the detector of the given wavelength, including responsivity, cold filter transmission and detector window transmission.

$$S(\lambda) = \frac{a_p \pi}{4(F/\#)} \Delta \lambda W_{\text{slit}} \tau_{\text{opt}}(\lambda) R(\lambda). \quad (\text{A.9})$$

$F/\#$ is the channels's F-number and a_p is the area of one detector pixel, $\Delta \lambda$ is the pixel spectral bandwidth, W_{slit} is the slit width, $R(\lambda)$ is the incoming radiance, $\tau_{\text{opt}}(\lambda)$ is transmission of the optics, which is the product of the transmission properties of all the optics, including the mirrors, lenses, AOTF ($\tau_{\text{opt}}(\text{AOTF})$), angular dependency and the echelle grating blaze function.

Although stated earlier, a clear distinction should be made between $S_{\text{electrons},n}$ and $S_{\text{electrons}}(i)$, both are different sources of electrons. $S(\lambda)$ and subsequently $S_{\text{electrons}}$ are used to simulate the shot noise, N_{shot} .

Appendix A.0.1. Thermal emission model

The thermal emission model employed in Ares follows that of [Thomas et al. \(2016\)](#). The total thermal background is difficult to calculate give that all components of NOMAD act as a blackbody radiation source, emitting thermal photons. Whilst no distinction is made in the thermal background estimation section of [Thomas et al. \(2016\)](#) it is stated that all the components are assumed to be at the same temperature as the instrument. Optical components within NOMAD are attached to a thermally conductive baseplate away from the heat generating central electronics board. Because of this the temperature of the optical parts, should not deviate more than a few degrees from the main instrument body. The calculation of the thermal background estimation is split into three ordered sections and is run for each detector pixel individually in the following manner:

1. From the optical components before the AOTF.
2. From the AOTF to the slit.
3. From the slit to the detector.

The thermal background contribution is modelled using the Planck function, and expressed as the power emitted per unit area per solid angle of NOMAD's component surface, at a given wavelength λ and temperature T :

$$B(\lambda, T) = \frac{2hc}{\lambda^5} \left(\frac{1}{\exp(\frac{hc}{\lambda k_b T}) - 1} \right). \quad (\text{A.10})$$

The number of emission generated electrons per wavelength, λ , from surface n is therefore given by,

$$S_{e^{-},n}(\lambda, T_n) = \varepsilon_n(\lambda) B(\lambda, T_n) \left(\frac{\lambda}{hc} \right) A \Omega \left(\prod_{j=n+1}^m \tau_j(\lambda) \right) E_R(\lambda) \Delta t, \quad (\text{A.11})$$

where $\varepsilon_n(\lambda)$ is the surface emissivity, $\left(\frac{\lambda}{hc} \right)$ is the energy of a photon of wavelength λ . $A \Omega$ is the instrument entendue. $\prod_{j=n+1}^m \tau_j(\lambda)$ is the cumulative transmission of all m optical elements between the surface and the pixel, $E_Q(\lambda)$ is the quantum efficiency of the detector and Δt is the observation time.

Firstly, the signal in electrons in the detector pixel i by thermal emission before the AOTF can be calculated as follows, summed over the n optical components, before the AOTF, and is given by,

$$S_{\text{tb1}}(i) = \sum_n \left(\frac{S_{\text{electrons},n}(\lambda_{i+1}, T_n) + S_{\text{electrons},n}(\lambda_i, T_n)}{2} \right) (\lambda_{i+1} - \lambda_i). \quad (\text{A.12})$$

Secondly, for components between the AOTF and the slit, the calculation becomes more complex, as all diffraction orders x need to be accounted for. For components between the AOTF and the slit, the thermal background noise is given by,

$$S_{\text{tb2}}(i) = \sum_n \sum_{x=0}^{\infty} \left(\frac{S_{\text{electrons},n}(\lambda_{x,i+1}, T_n) S_{\text{electrons},n}(\lambda_{x,i}, T_n)}{2} \right) \times (\lambda_{x,i+1} - \lambda_{x,i}). \quad (\text{A.13})$$

Thirdly, for the grating and components after the slit the signal in electrons is given by,

$$S_{\text{tb3}}(i) = \sum_n \int_{\lambda=0}^{\infty} S_{\text{electrons},n}(\lambda, T_n). \quad (\text{A.14})$$

Therefore, the total number of electrons generated in detector pixel i due to the thermal emission from NOMAD is given by,

$$S_{\text{tb}}(i) = \sum_{j=1}^3 S_{\text{tbj}}(i). \quad (\text{A.15})$$

The optical design of the NOMAD SO channel is such that it is composed of 7 elements, namely, the entrance optics, the AOTF filter, the spectrometer entrance slit, the collimating / imaging parabolic mirror, the echelle grating, the folding mirror and the detector. Returning to the problem of simulating N_{shot} and N_{tb} , we are faced with the challenge of defining all of the aforementioned terms.

As stated earlier, the signal arriving on the detector can be expressed as,

$$S(\lambda) = \frac{a_p \pi}{4(F/\#)} \Delta \lambda W_{\text{slit}} \tau_{\text{opt}}(\lambda) R(\lambda). \quad (\text{A.16})$$

The term $R(\lambda)$ is the incoming radiance from the Sun at Mars distance. This term is simulated with the Ares forward

model. τ_{opt} is the transmission of the optics, and is a product of the optics, mirrors, lenses, AOTF (τ_{AOTF}), the angular dependency and the echelle grating blaze function, given by,

$$\tau_{\text{opt}}(\lambda) = \prod_{j=n+1}^m \tau_j(\lambda). \quad (\text{A.17})$$

$F/\#$ is the channel's F-number, the F-number of an optical system is the ratio of the system's focal length to the diameter of the entrance aperture. The F-number is commonly indicated with the f/N format where N is the F-number. For NOMAD SO the limiting F-number is $f/5.12$, Neefs et al. (2015). Note that in Table 10 of Neefs et al. (2015) this is given for the cold

shield aperture as $f/3.936$. a is the area of one detector pixel, which Neefs et al. (2015) gives as $30 \times 30 \mu\text{m}^2$. $\Delta\lambda$ is the pixel spectral bandwidth, which can be determined from Equation 1 of Liuzzi et al. (2019). The size of the slit in the NOMAD SO channel is $60 \mu\text{m} \times 900 \mu\text{m}$, therefore $W_{\text{slit}} = 60 \mu\text{m}$.

Appendix B. Glossary

Appendix C. Abbreviations

Appendix D. Chemical Species

Appendix B. Glossary

Variable	Description	Example Equation(s)
m	AOTF diffraction order number.	1
p	Pixel number, $p \in [0, 319]$.	1
ν	Wavenumber in cm^{-1}	1
F_0, F_1, F_2	NOMAD SO p, ν, m relation coefficients.	1
G_0, G_1, G_2	NOMAD SO tuning relation coefficients.	1
A	AOTF frequency.	2
TF	AOTF transfer function.	3
ν_0	AOTF transfer function centre in cm^{-1} .	3
w	First zero crossing of sinc-squared function.	3
I_G	Gaussian amplitude of the AOTF transfer function.	3
ρ_G	Gaussian standard deviation of the AOTF transfer function.	3
q, n	AOTF transfer function continuum offset parameters.	3
I_0	Sinc-squared amplitude of the AOTF transfer function.	4
F_{sinc}	AOTF transfer function sinc-squared contribution.	4
F_{gauss}	AOTF transfer function Gaussian contribution.	5
F_{cntmn}	AOTF transfer function continuum contribution.	6
F_{blaze}	Blaze function.	7
p_0	Blaze function pixel centre in pixel units.	7
w_p	Blaze function width.	7
I_0, I_1	Blaze function p_0 relation coefficient.	8
PEC	<i>Partial Elements Continuum</i> .	9
PE	A <i>Partial Element</i> of the PEC .	9
δm	A discrete change in diffraction order m .	9
$AOTF$	AOTF transfer function at the AOTF frequency A , for spectral grid ν_j of diffraction order j .	10
$R(A, \nu_m)$	Observed Radiance by the NOMAD SO channel.	11
$R(j, \nu_j)$	Signal terms.	11
ν_j	Spectral grid of diffraction order j	10,11,12
$n_{\text{lat-lon}}$	Ares Geometry module grid point number.	
n_{layers}	Number of atmospheric layers.	
r_s	TGO observation altitude.	13,14,15
φ_s	TGO sub-observation longitude.	13,14,15
θ_s	TGO sub-observation latitude.	13,14,15
(x_s, y_s, z_s)	TGO Cartesian coordinate.	13,14,15
(x_t, y_t, z_t)	Tangent point Cartesian coordinates.	
\in	Set membership, read as <i>is an element of</i> .	
\forall	Universal quantifier, read as <i>for all</i> .	
r_{Mars}	Mars radius in km.	18
\mathbf{y}	Measurement vector.	22,28,29,30,31,32
\mathbf{x}	State vector.	22,28,29,30,31,32
\mathbf{b}	Parameter vector.	22
$\mathbf{F}(\mathbf{x}, \mathbf{b})$	Forward model.	22
ϵ	Error vector in the forward model	22
λ	Wavelength.	23,24,25,26,29
k_B	Boltzmann constant.	A.10
τ	Optical depth.	
$P(\mathbf{x}, \mathcal{M})$	pdf of \mathbf{x} for atmospheric forward model \mathcal{M} .	28,30
$P(\mathbf{y}, \mathcal{M})$	pdf of \mathbf{y} for atmospheric forward model \mathcal{M} .	28,30
$P(\mathbf{y} \mathbf{x}, \mathcal{M})$	pdf of \mathbf{y} given \mathbf{x} for atmospheric forward model \mathcal{M} .	28
$P(\mathbf{x} \mathbf{y}, \mathcal{M})$	<i>a posteriori</i> pdf of \mathbf{x} given \mathbf{y} for atmospheric forward model \mathcal{M} .	29
$\mathbf{0}$	Zero vector.	31
$\nabla_{\mathbf{x}}$	Gradient operator for \mathbf{x} .	31
$l(z)$	Optical path length.	24
N_m	Total number of absorbing species.	25
\mathcal{T}_λ	Monochromatic transmittance at wavelength λ .	26

Appendix B. Glossary (Continued)

Variable	Description	Example Equation(s)
dl_j	Atmospheric path lengths.	
a, b, c	Ellipsoid coefficients.	17
$r_{\text{Mars,p}}$	Mars polar radius in km.	18
$r_{\text{Mars,e}}$	Mars equatorial radius in km.	18
f	Ellipsoid flattening ratio.	18
Δz_i	Height of atmospheric layer i above the surface ellipsoid.	19,20,21
N	NOMAD total noise contributions.	A.1
N_{dark}	Dark noise.	A.1,A.2
N_{shot}	Shot noise.	A.1,A.7
N_{ro}	Readout noise.	A.1,A.3
N_{quant}	Quantisation noise.	A.1,A.5,A.6
N_{tb}	Thermal background noise.	A.1
Δt	Integration time in seconds.	A.2
$S_{\text{tb}}(i)$	Total number of electrons generated in detector pixel i due to instrument thermal emission.	A.4
$S_{\text{FWC}}(i)$	Detector pixel i full-well-capacity.	A.5
$\Delta V_{\text{ADC,usable}}$	Usable voltage range of the analogue-to-digital converter.	A.5
$\Delta V_{\text{ADC,max}}$	Maximum voltage range of the analogue-to-digital converter.	A.5
$S_{\text{electrons}}(i) = S(i)$	Number of electrons generated in detector pixel i during integration time, associate with calculating N_{shot} .	A.7
λ_i	Wavelength corresponding to pixel i .	A.8
$E_Q(\lambda_i)$	Detector quantum efficiency at λ_i .	A.8
$\tau_{\text{det}}(\lambda_i)$	Detector sensitivity at wavelength λ_i .	A.8
$F/\#$	Channel F-number.	A.9
a_p	Area of one detector pixel.	
$\Delta \lambda$	Pixel spectral bandwidth.	
W_{slit}	Detector slit width.	A.9
$R(\lambda)$	Incoming radiance.	
$\tau_{\text{opt}}(\lambda)$	Detector optics transmission.	A.9
$\tau_{\text{opt}}(\text{AOTF})$	AOTF optics transmission.	
$S_{\text{electrons,n}} = S_{e^-,n}$	The number of emission generated electrons per wavelength λ from surface n .	A.11
$\prod_{j=n+1}^m \tau_j(\lambda)$	Cumulative transmission of all m optical elements between the surface and the pixel.	A.11
$E_Q(\lambda)$	Quantum efficiency of the detector.	A.11
Δt	Observation time.	A.11
$S_{\text{tb1}}(i)$	Detector pixel i thermal emission signal in electrons before the AOTF.	A.12
$S_{\text{tb2}}(i)$	Detector pixel i thermal emission signal in electrons between AOTF and slit.	A.13
$S_{\text{tb3}}(i)$	Detector pixel i thermal emission signal in electrons between slit, grating and components.	A.14
$I_\lambda(z)$	The monochromatic intensity of radiation passing through a gas.	
$I_\lambda(0)$	The monochromatic intensity of radiation at the top of the atmosphere.	
$\tau_\lambda(z)$	Medium optical depth at altitude z .	
$\varepsilon_n(\lambda)$		
$A\Omega$	NOMAD instrument entendue.	A.11
T	Temperature in Kelvin (K).	
h	Planck constant.	A.8,A.10,A.11
c	Speed of light in a vacuum.	A.8,A.10,A.11
$B(\lambda, T)$	Planck function.	A.10
$\zeta_m(\lambda)$	Absorption cross-section at wavelength λ .	24
$\chi_m(z)$	Atmospheric column density for molecule m .	24
$\tau_\lambda(z)$	Total optical depth. 25	

Appendix C. Abbreviations

Variable	Description
NOMAD	Nadir and Occultation for MAars Discovery
TGO	Trace Gas Orbiter
ESA	European Space Agency
ppmv	parts per million per unit volume
ppbv	parts per billion per unit volume
pptv	parts per trillion per unit volume
RTM	Radiative Transfer Model
MSL	Mars Science Laboratory
SAM	Sample Analysis at Mars
TLS	Tunable Laser Spectrometer
FTS	Fourier Transform Spectrometer
RTE	Raditive Transfer Equation
MAP	Maximum A Posteriori
MCD	Mars Climate Database
PSA	Planetary Science Archive
GCM	Global Climate Model
NASA	National Aeronautics and Space Administration
BIRA-IASB	The Royal Belgian Institute for Space Aeronomy
ILS	Instrument Line Shape
HDF	Hierarchical Data Format
SNR	Signal to Noise Ratio
XML	Xtensible Markup Language
AOTF	Acousto Optic Tunable Filter
EAICD	Experiment to Archive Interface Document
SO	Solar Occultation
LNO	Limb Nadir Occultation
PFS	PPlanetary Fourier Spectrometer
MCMC	Markov Chain Monte Carlo
LOS	Line Of Sight
VMR	Volume Mixing Ratio
UVIS	Ultra Violet Infrared Spectrometer
FWHM	Full Width Half Maximum
PSG	Planetary Spectrum Generator
MGS	Mars Global Surveyor
MOLA	Mars Orbiter Laser Altimeter
DSK	Digital Shape Kernel
API	Application Programming Interface
HAPI	Hitran Application Programming Interface
NEMESIS	Non-linear Optimal Estimator for MultivariatE Spectral. AnalySIS.

Appendix D. Chemical Species

Symbol	Description
HCN	Hydrogen Cyanide
OCS	Carbonyl Sulfide
SO ₂	Sulfur Dioxide
NH ₃	Ammonia
HO ₂	Hydroperoxyl
HCl	Hydrogen Chloride
H ₂ S	Hydrogen Sulfide
H ₂ CO	Formaldehyde
N ₂ O	Nitrous Oxide
NO ₂	Nitrogen Dioxide
C ₂ H ₄	Ethylene (Ethene)
C ₂ H ₂	Acetylene (Ethyne)
HDO	Deuterium Oxide (Heavy water)
CH ₄	Methane
C ₂ H ₆	Ethane
C ₃ H ₈	Propane
δ ¹³ C	Delta Carbon Thirteen
δ ² H	D/H ratio
CO	Carbon Monoxide
CO ₂	Carbon Dioxide
H ₂ O	Water
O ₃	Ozone